Ammonia as a potential energy vector in the Burgeoning hydrogen economy

Abhishek Kumar, Vaibhav Vibhu, Jean-Marc Bassat, Lucy Nohl, L. G. J. de Haart, Marcel Bouvet, Rüdiger-a Eichel

ChemElectroChem

Review
doi.org/10.1002/celc.202300845

Chemistry Europe
European Chemical Societies Publishing

www.chemelectrochem.org

Ammonia as a Potential Energy Vector in the Burgeoning Hydrogen Economy

Abhishek Kumar[+],[a] Vaibhav Vibhu[+],*[b] Jean-Marc Bassat,[c] Lucy Nohl,[b] L. G. J. (Bert) de Haart,[b] Marcel Bouvet,*[a] and Rüdiger-A. Eichel[b, d]

The adoption of green hydrogen economy is an indispensable necessity in the current global scenario of environment and energy security. In this endeavor, ammonia is poised to play a key vector of hydrogen to mitigate the challenges arising from transportation, storage and safety. Besides containing a high volumetric and gravimetric hydrogen density, NH_3 decomposition into H_2 for onsite utilization as a distributed energy source is devoid of greenhouse gases production. In this endeavor, significant technological advancements have been made for *in situ* production of H_2 from NH_3 decomposition and the use of NH_3 in fuel cell devices to produce electricity. The ammonia decomposition methods to produce H_2 mainly involve thermocatalytic, oxidative, electrocatalytic and photocatalytic, among which the catalyst assisted thermal cracking of NH_3 has been widely investigated. The research progress in electrolysis of NH_3 has been notable in the last couple of years and provides a low-cost alternative to produce H_2 at room temperature. In the area of device development, solid oxide fuel cells (SOFC) have witnessed rapid development in the performances and stability, as ammonia is completely decomposed into H_2 and N_2 at high operating temperature above ~700 °C.

1. Introduction

Carbon neutrality is a key focus in the global energy system currently, in which minimizing the CO_x emission is essential to restrict the global temperature rise under 1.5 °C from the pre-industrial era. Although, the objective is indispensable to achieve, the current human efforts in terms of monetary investment and political will are not sufficient to accomplish the goal and studies are predicting that global warming will pass the limit of 1.5 °C in the coming years.[1] To mitigate the risk of global temperature rise, it is necessary to discourage the use of carbon-based fuels and increase the rapid adoption of energy sources/carriers with minimum or no carbon footprint on the environment. In this endeavor, different clean energy technologies are being explored, in which hydrogen have clearly stood out as a promising clean energy vector.[2,3] At first, it promises to provide a clean fuel solution to the automobile sector, accounting for 23% of total CO_2 emission.[4] Hydrogen fuel cell-based vehicles are already witnessing commercialization with extended range up to 400 km.[5,6] Moreover, hydrogen can be used as a distributed energy source where electricity derived from renewable energy is hard to access or lacks certainty of continuous supply. The high interest in hydrogen is inspired from its high gravimetric energy density; 120 MJ kg^{-1}, zero emission of CO_x gases upon utilization and technology maturation for the large scale sustainable production.[7] Thus, hydrogen has become a preferred choice for the future energy market, experiencing a rapid growth in its production. The demand of hydrogen is expected to surpass 150 Mt annually in the global energy network by 2030 to achieve the target of net-zero emission by 2050,[8,9] which has prompted the policy makers globally to tune the political agenda to fiscally incentivize the hydrogen economy and expand its outreach. However, there are existing hurdles in the current hydrogen economy, related to transportation, distribution and storage of hydrogen, hampering its integration in the global energy network. Despite, possessing a very high gravimetric energy density, the volumetric energy density of H_2 is very low; 9.8 kJ/L at room temperature and atmospheric pressure, which is many times inferior to existing fuels like gasoline (15.8 MJ/L).[10] Thus, it makes impractical to use H_2 gas at ambient conditions as a source of energy. Storage at high pressure (200 bar) and liquification of H_2 (at −250 °C) are some earlier investigated strategies, but they are very expensive and not feasible at large scale, owing to high input energy required to attain very high pressure and extremely low temperature. Additionally, in such harsh conditions, H_2 can damage the storage tank and can cause explosion upon leak,[11,12] thus posing a serious concern for public safety.

[a] *A. Kumar,[+] M. Bouvet*
Institut de Chimie Moléculaire de l'Université de Bourgogne, UMR CNRS 6302,
Université Bourgogne, Dijon, France
E-mail: marcel.bouvet@u-bourgogne.fr

[b] *V. Vibhu,[+] L. Nohl, L. G. J. de Haart, R.-A. Eichel*
Institute of Energy and Climate Research, Fundamental Electrochemistry (IEK-9), Forschungszentrum Jülich GmbH, 52425 Jülich, Germany
E-mail: v.vibhu@fz-juelich.de

[c] *J.-M. Bassat*
CNRS, Université de Bordeaux, Institut de Chimie de la Matière Condensée de Bordeaux (ICMCB), 87 Av. Dr. Schweitzer, F-33608 Pessac Cedex, France

[d] *R.-A. Eichel*
Institute of Physical Chemistry, RWTH Aachen University, 52074 Aachen, Germany

[+] *These authors contributed equally to the publication.*

Abhishek Kumar Abhishek Kumar is a postdoctoral researcher at Burgundy University. He is working on porous metal nanostructures and molecular materials for electrocatalytic and sensing applications. He received Ph.D at Clermont Auvergne University, while working on mass sensors development for VOCs detection. He was a recipient of FAPESP postdoctoral fellowship (2016/07461-1) at Sao Paulo University to pursue research on nanoporous metal and molecular catalysts for their applications in energy and sensors technologies. He is a member of International Society of Electrochemistry. He was awarded a prize from Club Microcapteurs Chimiques (CMC2) de France in 2020 for his contribution in gas sensors research.

Vaibhav Vibhu studied chemistry and obtained his master's degree from the University of Delhi and the University of Grenoble Alpes. He then completed his Ph.D. in 2016 at the ICMCB-CNRS, University of Bordeaux, France, on "Stability and ageing studies of praseodymium-based nickelates as cathodes for SOFCs". Afterward, he moved to IEK-9 at Forschungszentrum Jülich, Germany, to continue his work in the field of solid oxide cells (SOFCs/SOECs). His research focuses on the development of Solid Oxide Cell (SOC) materials, materials characterizations and processing, the manufacturing of cells, electrochemical characterizations and the identification of reaction mechanisms of electrodes and degradation phenomena of cells.

Jean-Marc Bassat prepared his Ph.D. at the LCS - CNRS lab (Bordeaux, 1986) then his HDR (1995) on the 2D electrical properties of oxides especially at high T°/function of pO_2. He has mainly worked at the ICMCB – CNRS laboratory as a CNRS researcher, then as a senior scientist. From 2022 he occupied part of his time a position of scientific delegate in the field of "Energy and Hydrogen" at the CNRS – Chimie Institute of CNRS. His research interests are in the field of materials for Solid Oxide Fuel/Electrolysis Cells (oxides with electronic and ionic transport properties), thick layers deposition methods (tape-casting, screen-printing, infiltration), advanced characterizations methods in link with the electrochemical properties of the materials/cells (isotopic oxygen exchanges, impedance spectroscopy measurements, electronic relaxation measurements, (I,V) curves measurements for instance).

Lucy Nohl studied chemistry with a focus of electrochemistry and materials at RWTH Aachen. She conducted her Ph.D. studies on the topic of high-temperature co-electrolysis of steam and carbon dioxide to syngas in the Institute of Energy and Climate Research – Fundamentals of Electrochemistry at Forschungszentrum Jülich. Her research interests are the analysis of mechanisms and reactions during the electrolysis and fuel cell processes by use of impedance spectroscopy and the long-term stability of the cells by current-voltage characteristics and post-test characterization. The aim is to optimize cells and materials for later use in the stacks and systems.

L.G.J. (Bert) de Haart (*1958) studied Chemistry at the State University of Utrecht (The Netherlands) and obtained his Master Degree with specialty Solid State Chemistry in 1981. In 1985 he obtained his PhD Degree also from the State University of Utrecht. From 1987–1992 he was research assistant (Post-Doc) at the University of Twente (The Netherlands) in the Department of Chemical Technology. In 1992 he joined the Forschungszentrum Jülich (Germany) where he continued his work on the development of Solid Oxide Fuel and Electrolysis Cells (SOFC/SOEC) with emphasis on materials development and cell- and stack-design, -manufacturing and -characterization.

Marcel Bouvet prepared his Ph.D. at the ESPCI (Paris) on the electrical properties of phthalocyanines (1992). He has worked mainly at the ESPCI as an associate professor, but also at the University Pierre and Marie Curie (UPMC, Paris) and the University of Connecticut (USA). He started a full professor position at the University of Burgundy (Dijon, France) in 2008 where he is currently the head of the department Synthesis, Environment and Materials (SEM) in the ICMUB. His research interests are in the field of molecular materials, conductometric transducers, organic electronics, and chemical sensors.

Rüdiger-A. Eichel holds a chair for Energy Conversion and Storage at RWTH Aachen University, Germany, as full professor. In a joint appointment, he acts as scientific director of the Institute of Energy and Climate Research (IEK-9) at Forschungszentrum Jülich, Germany. Prof. Eichel earned his diploma in solid-state physics at the University of Cologne, Germany, and obtained his Ph.D. degree in physical chemistry at the Swiss National Institute of Technology (ETH) in Zürich, Switzerland. Prof. Eichel was qualified as a university lecturer (venia legendi) in Physical Chemistry at Darmstadt Technical University with a habilitation thesis on "Nanoscale properties of functional ceramics". Current research interests focus on electrochemical energy conversion and storage technologies and their integration in sustainable value chains.

A potential solution to the distribution and storage challenge of hydrogen is to convert it into another compound, which is stable and easy to handle in the ambient conditions, at the production site, from where it can be further stored or transported and can be finally regenerated into H_2 at the site of utilization. There are several hydrogen vectors, which are being investigated for large-scale application, such as methanol, metal hydrides, metal organic frameworks (MOF) and ammonia. Methanol and ammonia have drawn wider interests because of their higher hydrogen storage capacity, large scale production and their storage and transportation using the existing infrastructures, like pipelines, ships or trucks. However, regeneration of H_2 from methanol produces CO_x gases, which is not desired for a green hydrogen economy. On the other hand, ammonia is a carbon-free carrier of H_2, having one of the highest gravimetric (17.8%) and volumetric (121 kg H_2 m^{-3} at 10 bar) hydrogen density (Figure 1a) among other H_2 carriers and can be liquefied at room temperature at a mild condition (8.6 bar). There are established methods for large-scale industrial production of ammonia, mainly the Haber-Bosch process, in which N_2 and H_2 are combined at high pressure (20 bar) and temperature (ca. 400 °C) in the presence of an iron-based catalyst to achieve more than 90% yield of NH_3. Moreover, there are established transport and storage infrastructures for NH_3, which would ensure its rapid integration in the hydrogen economy. A recent techno-economic study revealed that hydrogen economy based on NH_3 vector has the lower source to tank cost (source to end use) of producing and utilizing carbon-neutral hydrogen from those based on compressed H_2 and methanol.[13] Figure 1b clearly highlights that gasoline gallon equivalent (GGE) price of H_2 in NH_3 based hydrogen economy is 31% and 18% lower than compressed H_2 and methanol-based hydrogen economy, respectively. Higher cost in compressed H_2 based hydrogen economy is mainly attributed to distribution, dispensation and transmission of H_2, while carbon capture in methanol based H_2 production accounts significant expenses.

The role of ammonia in a sustainable green hydrogen economy is depicted in Figure 1c. The traditional Haber-Bosch process is highly energy intensive and produces large amount of CO_2, mainly in the H_2 production from natural gas by steam reforming, which is not favorable for achieving the net-zero emission target. In a modified Haber-Bosch process, electricity derived from renewable sources can be used to operate the electrolysers for water splitting to produce green hydrogen,

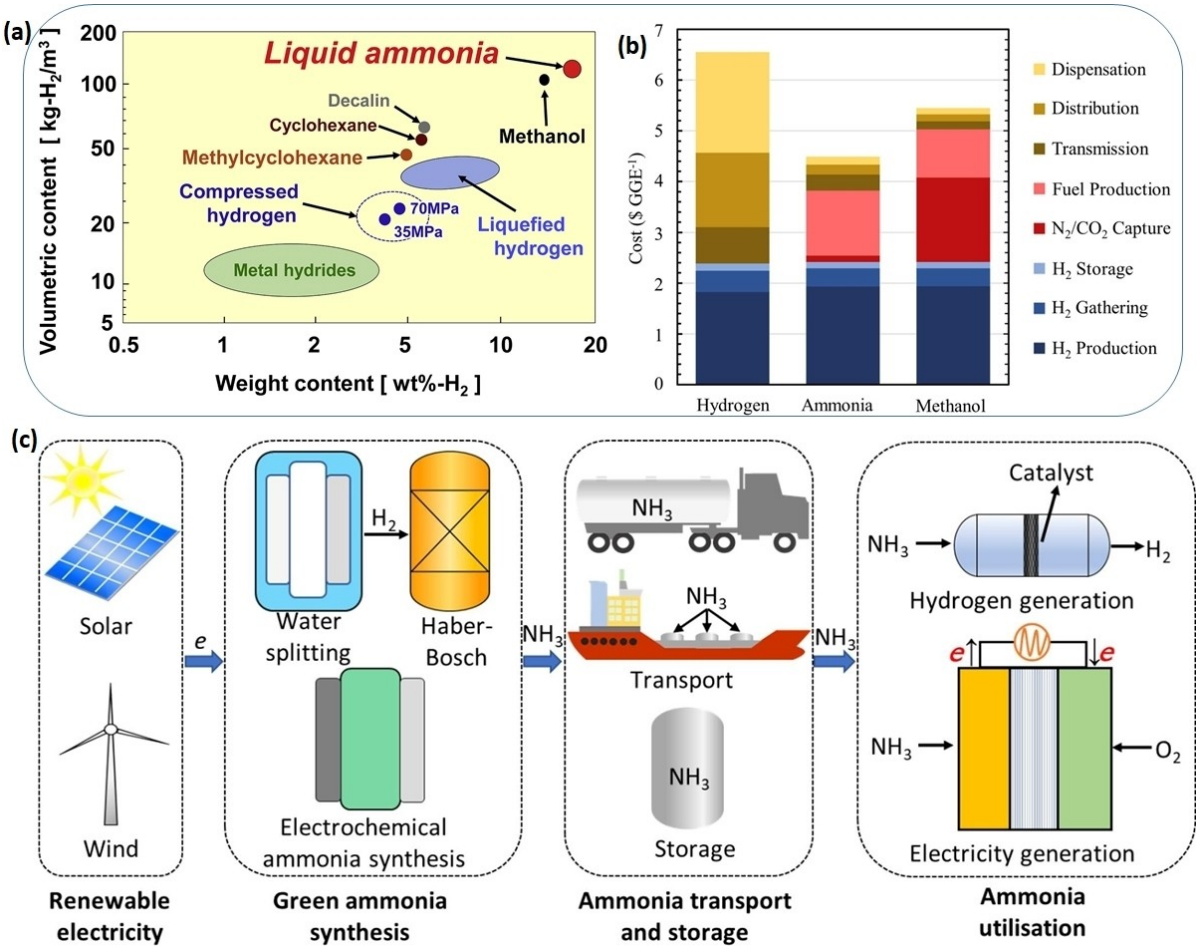

Figure 1. (a) Comparison of volumetric and gravimetric H_2 content in different compounds. Reproduced with permission.[14] Copyright 2021 Elsevier. (b) Comparison of the source of tank cost hydrogen economy based on compressed H_2, NH_3 and methanol. Reproduced with permission.[13] Copyright 2019 Elsevier. (c) Schematic representation of adoption of green ammonia as a vector of hydrogen. Reproduced with permission.[15] Copyright 2021 Elsevier.

which is subsequently used to produce NH_3. Indeed, the green H_2 production has witnessed tremendous technological advancements and its share in the total H_2 production is steadily increasing in recent years.[10,16] The ammonia so produced can be transported over the long distance or stored in the liquid form through the existing transportation logistics. NH_3 can be finally decomposed onsite in a suitable reactor to produce green hydrogen, which can be used in different applications, such as power generation, fuel cells and refueling stations.

The last stage of the NH_3 based green hydrogen economy, *i.e.* NH_3 decomposition step to regenerate H_2 has garnered multitudes of academic and industrial research interests to design efficient, robust and low-cost technologies. In the light of the recent advances in this field, at first, the present review gives a brief overview of different methods explored for ammonia decomposition reaction, such as thermal, photochemical, electrochemical and oxidative cracking in the presence of a catalyst. Among these methods, thermocatalytic based approaches have been extensively studied and plenty of recent reviews are available focused on catalytic materials and reactors.[17–20] However, the electrochemical-based method, involving the electrooxidation of NH_3 at room temperature[21] is a relatively new approach and analysis of recent development in this area is limited. Therefore, the advancements made in the electrooxidation methods of NH_3 by different metals and molecular catalysts are reviewed in detail. The second part of the review reports the recent progress made in the development of direct NH_3 fuel cell devices and enlists the advantages and limitations over the low temperature H_2 fuel cell devices, in which H_2 is produced at room temperature by NH_3 electrooxidation. Finally, some perspectives about the future research directions are proposed to overcome pertaining challenges of NH_3 based hydrogen economy.

2. Advancements in NH_3-to-H_2 Conversion Technologies

The decomposition of NH_3 to produce H_2 is a key step for the success of a carbon neutral and cost-effective hydrogen economy. In this direction, different technologies are being investigated and significant advancements have taken place in four technologies for NH_3-to-H_2 conversion (Figure 2). The chemical route-based methods involve thermocatalytic cracking and oxidative reforming of NH_3 to produce H_2. In the thermocatalytic approach, ammonia is fed into a reactor having a catalytic bed maintained at high temperature (in the range of 400 to 600 °C) to decompose it into N_2 and H_2, which are collected at the output and then separated/purified to obtain

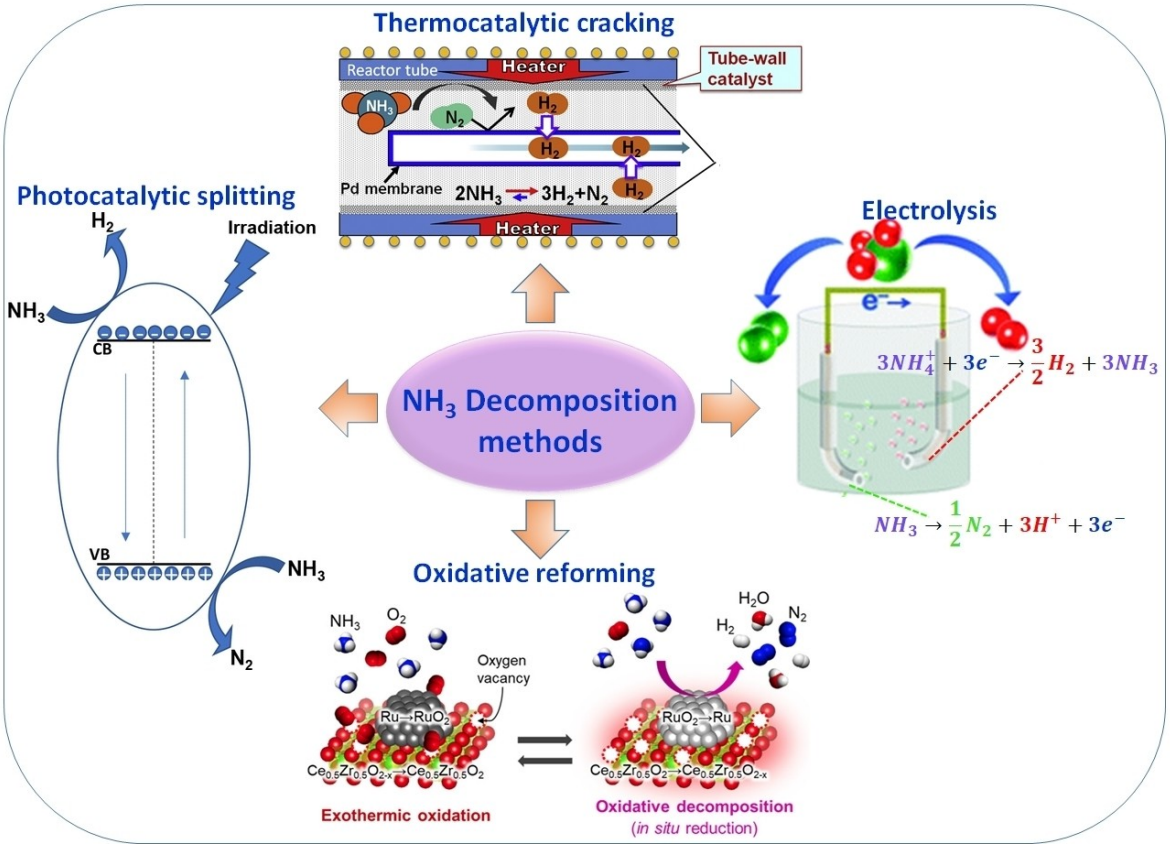

Figure 2. Different technologies investigated for the decomposition of NH_3 into H_2 and N_2 based on chemical (Reproduced with permission.[14,23] (Copyright 2021 Elsevier, Copyright 2020 ACS), electrocatalytic (Reproduced with permission.[24] Copyright 2015 RSC)) and photocatalytic approaches. Reproduced with permission.[25] Copyright 2023 ACS.

clean H_2. In this method, the reactor temperature, its design and the nature of catalytic formulation play a pivotal role in the NH_3 conversion efficiency. Oxidative reforming is another chemical approach developed to overcome the issue of high temperature required in the thermocatalytic cracking, as it operates at room temperature and is thus less energy intensive. In this method, a mixture of NH_3 and O_2 is passed over a pre-treated catalytic surface, over which NH_3 is adsorbed, causing an increase in the temperature of the catalytic layer. On the heated catalytic bed, NH_3 is oxidized in the presence of O_2, which is an exothermic process, resulting in the further increase of temperature of the catalytic layer, sufficient to induce cracking of NH_3 into N_2 and H_2. Thus, the heat required for the endothermic decomposition of NH_3 is supplied in situ by the exothermic oxidation of NH_3. Thus, the reactor does not need external heating and it can be operated at room temperature. However, the pre-treatment of the catalyst surface requires heating at ca. 300 °C. To lower the cost incurred by the use of high temperature, technologies operating at room temperature have been developed for NH_3 splitting into H_2 and N_2. The photocatalysis based method is one of these approaches, in which light irradiation of the catalyst surface generates electrons (e^-) and holes (h^+) in the conduction band (CB) and valence band (VB) of the material. The photogenerated electrons and holes cause oxidation of NH_3 to produce H_2 and N_2. The NH_3 conversion efficiency depends on the band gap of the semiconducting catalytic materials and pH of the reaction medium. Electrolysis of liquid NH_3 is a low-energy demanding method to produce clean H_2 at room temperature, considering that thermodynamic voltage of NH_3 electrolysis is 0.077 V (with reference to NHE).[22] It means that electrolysis of liquid ammonia requires 94% less energy than the splitting of H_2O, which electrolysis voltage is 1.23 V (with reference to NHE). That is why, it has garnered significant interest in recent years and it is a potential perspective in the future hydrogen economy. In this method, NH_3 is electrochemically oxidized into N_2 on the anode, producing protons and electrons. The protons migrate to the cathode, where they are reduced to produce H_2. The method requires the use of electrocatalysts and a suitable electrolyte to attain higher efficiency.

The photo and electrocatalytic conversion of NH_3 into H_2 offers many advantages over the conventional thermal cracking of NH_3 to produce H_2. Photo and electrocatalytic based methods are operated at room temperature and at atmospheric pressure, making them highly energy efficient from the operational point of view. On the contrary, the thermal cracking requires a continuous heating to maintain a temperature around 400–600 °C and is operated at a low pressure,[26] making it highly energy inefficient. Moreover, thermal cracking uses a large amount of expensive Ru-based catalyst, which is a scarce and expensive metal. Photo and electrocatalytic approaches on the other hand are using cheaper oxides-based semiconductor (TiO_2 and ZnO) and transition metal based electrocatalysts. Other potential advantages of photo and electrocatalytic methods are high conversion efficiency and formation of the pure product, while thermal cracking uses a separation membrane to isolate the pure H_2. However, despite multiple advantages of photo and electrocatalytic methods over the thermal cracking, their upscaling is not yet achieved unlike the thermal cracking method. In photocatalytic decomposition, generation of the nitrogen oxide can be a risk in some photocatalysts and lower the H_2 yield.

2.1. Thermocatalytic Cracking of NH_3

Thermocatalytic conversion of NH_3 into H_2 is the most extensively investigated method and is based on the fact that the decomposition of NH_3, as indicated in the equation 1 is an endothermic process, requiring a large heat of reaction. The reaction is thus favored at high temperature and low pressure. It has been previously reported that NH_3 conversion efficiency is temperature dependent in the range of 250–450 °C (Figure 3a) and there is no effect of temperature thereafter.[27] However, the complete conversion is achieved at a temperature of ca. 650 °C in real conditions. The process is highly dependent on the kinetics of the reaction above 450 °C, which is strongly modulated by the nature of the catalysts and the ammonia interaction with them. To lower the decomposition temperature of NH_3, several catalysts have been used in combination with large area support and reaction promoters.

$$2NH_3 \rightarrow N_2 + 3H_2 \quad \Delta H^{\circ}_{298\ K} = 46.22\ kJ/mol_{NH3} \tag{1}$$

Figure 3b depicts the comparison of ammonia conversion efficiency and H_2 production rate of different metal nanoparticles. Notably, Ru-based catalysts have demonstrated the highest NH_3 conversion as well as the highest H_2 production rate at 450 °C and 0.1 bar among different metals.[28] Indeed, multiple reviews have been reported recently, highlighting the progress made in Ru-based catalysts, especially in reducing Ru-content and the reaction temperature, in NH_3 decomposition reaction to produce hydrogen.[29–32] Additionally, Ru catalytic activity strongly depends on the type of support and on the reaction promoters. The large area support material and its strong interaction with Ru facilitate the efficient dispersion, exposure and prevention of agglomeration and leaching of Ru particles during the harsh reaction conditions. Traditionally, metal oxides, such as Al_2O_3, MgO, TiO_2, CeO_2 and ZrO_2 were mainly used as support, but recently, many carbon-based supports, such as carbon nanotube (CNT), graphene, activated carbons as well as mesoporous materials, like silica and spinels have been investigated. Interestingly, the activity of metal particles varies in different manners, depending on the type of selected support. For instance, over an alumina support, the relative activity decreases in the order $Ru > Ni > Rh > Co > Ir > Fe \gg Pt > Cr > Pd > Cu \gg Te$, Se, Pb,[33] while over the CNT support the catalytic activity follows the trend $Ru > Rh \approx Ni > Pt \approx Pd > Fe$.[34] Moreover, the catalytic activity is further enhanced by performing heteroatom doping in the CNT or graphene-based support.[35] On the effect of different supports for the same catalyst, the work of Yin et al. reported that catalytic activity of Ru, dispersed over different supports, decreases in the order of $CNTs > MgO \gg TiO_2 > Al_2O_3 > ZrO_2 >$

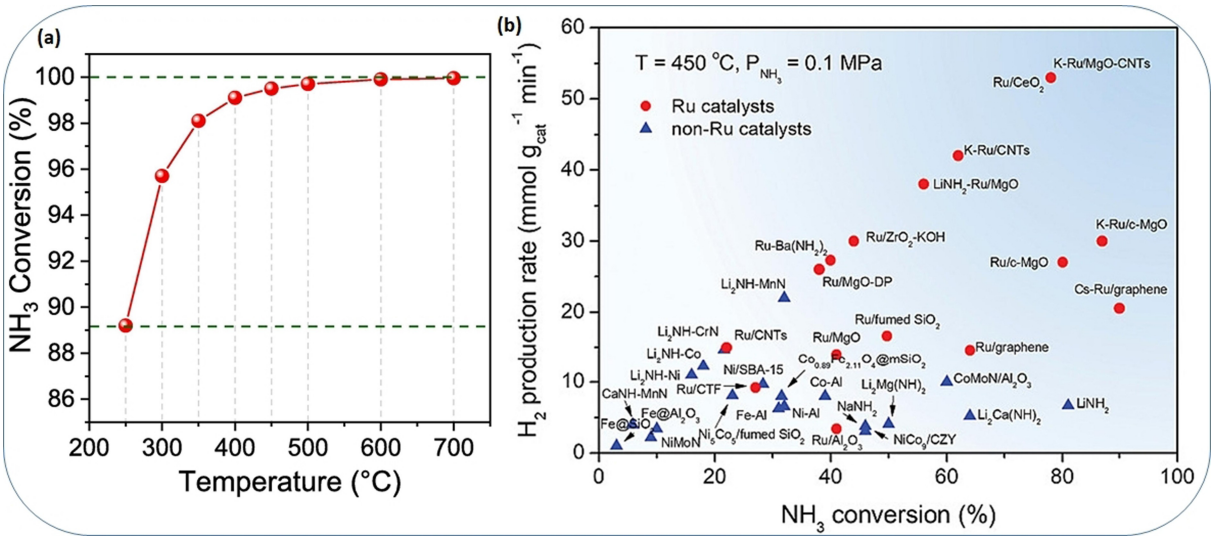

Figure 3. (a) Thermodynamic evolution of ammonia conversion into H_2 and N_2 as function of temperature. Reproduced with permission.[10] Copyright 2023 Elsevier. (b) Comparison of NH_3 conversion efficiency and H_2 production rate for different metal catalysts. Reproduced with permission.[28] Copyright 2021 Wiley.

activated carbons.[34] The higher activity of the Ru particles supported on CNT was attributed to their improved dispersion on the large active surface of the support. Indeed, the presence of oxygenated functional groups, such as carboxylic and hydroxyl groups facilitate stable anchoring of the metal particles on the CNT support and prevent their agglomeration during the catalytic operation. On the other hand, dispersion of Ru particles on the metal oxides support is not efficient, owing to poor electronic interaction, resulting in agglomeration of the Ru particles. Moreover, high electronic conductivity of CNT allows a faster electron transfer between the catalyst and the support and thus favors the desorption of N_2 from the catalyst surface, which is a critical step to regenerate the catalyst surface for further adsorption of NH_3. In the catalytic formulation of NH_3 decomposition, an electronic promoter is often used to accelerate the kinetics of the reaction. It facilitates the desorption of reaction intermediates, such as N_2 through transfer of electron in the antibonding orbital of the metal catalyst. Alkali and alkaline earth metal salts have been commonly used as promoters because of their high basic nature. The activity of Ru based catalyst strongly depends on the type of promoters present in the catalytic formulation and follows the trend as K > Na > Li > Ba > Ca.[36]

It is also worth noting that the activity of the metal catalysts for NH_3 decomposition also depends on the particle size, type of the active sites' exposure, orientation of the facets and the shape of the particles. The influence of the catalyst particle size on the NH_3 conversion is not consistent in all the reported literature. However, for Ru-based catalysts, the particle size in the range of 3–7 nm is considered optimal to achieve high conversion efficiencies.[37,38] The nature of the active sites of Ru-based catalysts also affects the kinetics of NH_3 decomposition. The B5 active site, comprising 3 atoms at the top and 2 atoms in the interior, revealed the highest activity.[37] Exposure of B5 active sites is controlled by the shape and crystalline orientation of the support materials.[39,40]

Although Ru based materials displayed the best catalytic activity in the NH_3 decomposition, it is a rare earth metal, making it expensive and unviable for H_2 production on an industrial scale. Therefore, the recent research focus has been shifted to develop non-noble monometallic and bimetallic catalysts. Among monometallic non-noble metal catalysts Ni, Fe and Co-based materials have shown high activity, although a higher reaction temperature is needed compared to Ru-based materials.[17,41] In particular, Ni-based catalysts have been extensively investigated and some of them are commercially available. It was found that rare earth elements, when used as a promoter with Ni supported on Al_2O_3, had a synergic improvement in the catalytic activity in the order of La ≈ Pr ≈ Nd > Y > Sm > Eu ≈ Gd > Ce.[42] Interestingly, Ni- based catalysts have shown higher activity on metal oxides supports and inferior activity on carbon-based supports, such as CNT, graphene oxide and activated carbon, which is an opposite trend compared to Ru-based catalysts.[17] To reduce the NH_3 decomposition temperature, while maintaining the high conversion efficiency, bimetallic catalysts are highly effective. Among an extensive series of bimetallic catalysts investigated, Ru–Ni, Ru–Co and Ru–Fe dispersed over an oxide support have demonstrated very high NH_3 conversion efficiency and turnover frequency (TOF) associated to hydrogen production rate as high as 80 s^{-1}.[43,44] Thus, such catalytic materials are a good alternative to reduce the expensive Ru content. Elsewhere, a recent study by Xie et al. reported Ru-free quinary material made of CoMoFeNiCu nanoparticles, which demonstrated nearly 100% NH_3 conversion and TOF associated to H_2 production rate higher than 25 s^{-1} at a temperature 500 °C,[45] which are comparable or better than Ru-based catalysts. Moreover, the catalysts showed ca. 20 times higher resistance to deactivation, compared to Ru-based materials.

2.2. Oxidative Reforming of NH_3

Ammonia oxidative reforming method has been explored in recent years as an alternative to conventional thermal cracking of NH_3, as it promises to decompose NH_3 at the ambient temperature. In this method, a fraction of the input NH_3 is oxidized, which is an exothermic process (equation 2 and 3), to generate sufficient heat for the endothermic NH_3 decomposition. Thus, the catalytic cycle within a closed reactor remains self-sustained without any external heat requirement. The heat generated in the exothermic oxidation of NH_3 depends on the proportion of O_2 added in the input with NH_3, however the amount of O_2 must be kept below 0.75 mole per mole of NH_3, in order to ensure production of H_2.

$$NH_3 + 0.25O_2 \rightarrow H_2 + 0.5N_2 + 0.5H_2O, \quad \Delta H = -75\ kJ/mol \tag{2}$$

$$NH_3 + 0.75O_2 \rightarrow 0.5N_2 + 1.5H_2O, \quad \Delta H = -317\ kJ/mol \tag{3}$$

Nagaoka et al. reported oxidative reforming of NH_3 by using RuO_2 nanoparticles dispersed on a γ-Al_2O_3 support.[46] Figure 4 exhibits the scheme of the self-sustained catalytic cycle, in which a mixture of O_2 and NH_3 is passed over RuO_2/γ-Al_2O_3 catalytic bed, which was pretreated by heating at 300 °C. Such pretreatment of the catalyst is necessary to remove the adsorbed H_2O, which otherwise competes with the adsorption of NH_3 and O_2. Over the catalyst surface, NH_3 is oxidized through an exothermic reaction (equation 2 and 3), inducing a localized heating of the catalytic bed. The temperature can exceed beyond 300 °C by controlling the input NH_3 and O_2 ratio. Thus, it provides a favorable condition for the decomposition of NH_3. The study revealed an ammonia conversion efficiency of *ca.* 99% and a production of H_2 of 67%, which are better performances than the thermal cracking of NH_3 using Ru-based catalysts. A bimetallic catalyst Ru–Cu dispersed on alumina support was also investigated for the oxidative decomposition of NH_3, which exhibited 3-times and 14-times higher activity than the individual Ru and Cu nanoparticles on the alumina support, respectively.[47] The nature of the support strongly influences the pretreatment temperature of the active catalyst. In this direction, different support materials were investigated with the objective to lower the pretreatment temperature. Interestingly, in the recent work of Matsunaga et al., a non-stoichiometric $Ce_{0.5}Zr_{0.5}O_{2-x}$ support was used to disperse Ru nanoparticles, which did not require any thermal pre-treatment, thus converting the NH_3 into H_2 at 25 °C with very high efficiency.[23] Despite requiring the low temperature, the key disadvantage of oxidative reforming of NH_3 is that it uses the expensive Ru metal, and so can not be scaled up to industrial scale. Additionally, there is risk of NO_2 production during the NH_3 oxidation reaction, which is hazardous for the environment.

2.3. Photocatalytic Splitting of NH_3

The splitting of NH_3 into H_2 and N_2 at room temperature through light irradiation is a highly promising strategy to develop a low-cost method for hydrogen production. In this method, a photocatalyst, typically a semiconducting material is used, which upon the light irradiation produces photoexcited h^+ in VB and e^- in the CB as shown in equation 4. The NH_3 is oxidized by the VB h^+, producing protons, (equation 5) which are reduced into H_2 by CB e^- (equation 6).

$$Photocatalyst + light \rightarrow e^- + h^+ \tag{4}$$

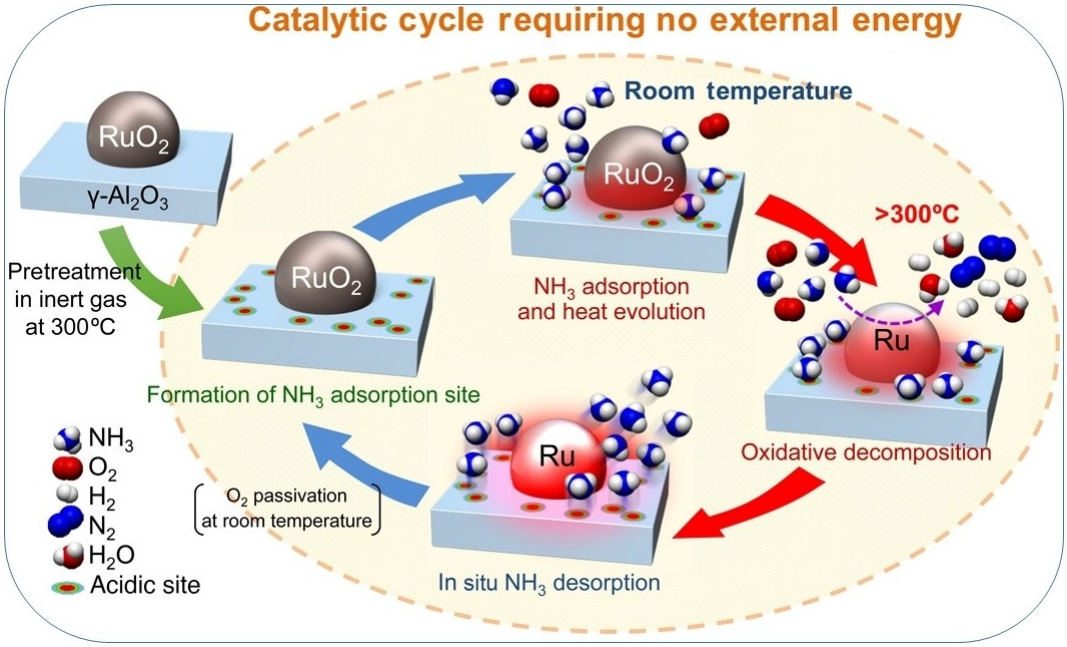

Figure 4. Schematic representation of the self-sustained catalytic cycle for the oxidative decomposition of NH_3 on a RuO_2/γ-Al_2O_3 catalytic bed. Reproduced with permission.[4]. Copyright 2017 Science.

$$2NH_3 + 6h^+ \rightarrow N_2 + 6H^+ \quad (5)$$

$$6H^+ + 6e^- \rightarrow 3H_2 \quad (6)$$

Thermodynamically, oxidation and reduction potential of NH_3 must lie between the VB and CB of the photocatalysts in order to achieve the decomposition of NH_3. In designing a photocatalyst, emphasis is given to promote the charges separation by inhibiting e^- and h^+ recombination. One of the widely adopted strategy is to use semiconducting materials loaded with metal nanoparticles, which form a Schottky contact because of the workfunction differences with an energy barrier ϕ_B at the metal-semiconductor junction (Figure 5a). Such Schottky contact facilitates separation of the photogenerated e^- and h^+, which are necessary to achieve high photocatalytic activity in the NH_3 splitting. Upon light irradiation, photogenerated e^- in the semiconductor CB migrates to the metal, which ease or difficulty are determined by the ϕ_B, which in turn is modulated by suitable choice of the semiconductor band gap and metal workfunction. TiO_2 has been extensively studied to develop photocatalysts for NH_3 splitting,[48,49] which is inspired from its low cost, high chemical stability, low toxicity and tunable bandgap. Kaneko et al. investigated platinized TiO_2 powder with 1 % Pt content for the H_2 production in a basic 1 % aqueous NH_3 solution by irradiating with UV light.[50] The expected redox reactions at anode and cathode are depicted in the Figure 5b, producing N_2 and H_2, respectively. The gas chromatography analysis of the products revealed the H_2 and N_2 content in the stoichiometric ratio of 3 : 1. The effect on the hydrogen production rate and of the overpotential of different metal nanoparticles loading on the TiO_2 powder was investigated.[51,52] It was found that among Cu, Ni, Au, Pd, Rh and Pt, hydrogen production rate increases with increasing workfunction of the metal (Figure 5c). Thus, Pt-loaded TiO_2 displayed the highest H_2 production rate as well as the lowest overpotential for the proton oxidation (Figure 5d). Such variations in the photocatalytic activities of TiO_2 with different metals are explained by looking at the alignment of its CB and VB with respect to the workfunction of the metal. In the Figure 5e, CB (−0.16 V) and VB (2.94 V) of TiO_2 and the workfunction of different metals are compared on the same reference potential scale to emphasize the ease of electron transfer at the semiconductor-metal junction. Notably, metal with larger workfunction (lower Fermi energy level) would easily accept electron from the conduction band of TiO_2. Thus, it is clear that Pt will accept the electrons from TiO_2 most easily and would facilitate the charges (e^- and h^+) separation by inhibiting the e^- and h^+ recombination, which is a key requirement for the higher photocatalytic activity.

Shiraishi et al. reported an Au–Pt bimetallic catalyst (10 mol % Au + 90 mol % Pt) loaded on TiO_2 for the photocatalytic splitting of aqueous solution of NH_3 under UV light exposure.[53] It was found that the bimetallic catalyst loaded TiO_2 displayed higher photocurrent than the Pt-loaded TiO_2, which was attributed to the lowering in ϕ_B at the junction, facilitating separation of photogenerated e^- and h^+. Besides TiO_2, other semiconducting materials, such as ZnO, C_3N_4, MoS_2 and ZnS[54,55] have been used for the NH_3 decomposition. However, their photocatalytic activity remains lower than that of TiO_2 based materials. Hybrid materials based on graphene have been explored for NH_3 photocatalytic decomposition. Among these materials, hybrid of TiO_2 nanowires intercalated with reduce graphene oxide[56] and MoS_2 with N-doped graphene[49] are worth mentioning,. The former was used with UV-light irradiation, while the latter was used with IR light exposure, and both exhibited a very high NH_3 decomposition efficiency into H_2. Elsewhere, Zhang and coworkers reviewed the recent advancements in the heterostructure materials development for the photocatalytic NH_3 conversion.[49]

Although, photocatalytic decomposition of NH_3 is a highly promising method to produce H_2 at room temperature, its efficiency remains very low to perceive commercial scale H_2 production. Moreover, higher activity has been achieved with Pt based catalysts, which is not sustainable for upscaling. Therefore, low-cost photocatalysts based on non-noble metal and organic material should be developed.

2.4. Electrolysis of NH_3 for Hydrogen Production

Electrochemical conversion of NH_3 into H_2 has attracted widespread research interests in the last few years and notable advancements have been reported.[57–60] While the major research focus has been the study of electrooxidation of NH_3 in aqueous solution, significant interests have emerged in the electrolysis of liquid ammonia in the last couple of years. This is motivated by the higher energy density of liquid NH_3, which has concentration of 40 M NH_3 at STP, three times higher than the saturated solution of NH_3 in water.[24] Additionally, aqueous alkaline solutions of NH_3 are highly corrosive for metallic containers, thus pose a big storage challenge. The redox reactions at the cathode and anode are different in the two cases. In the aqueous NH_3 electrolysis, NH_3 is oxidized at the anode in the presence of OH^-, producing N_2 and H_2O (equation 7), while the reaction at the cathode is the typical hydrogen evolution reaction in the basic medium (equation 8).

$$2NH_3 + 6OH^- \rightarrow N_2 + 6H_2O + 6e^- \quad (7)$$

$$6H_2O + 6e^- \rightarrow 3H_2 + 6OH^- \quad (8)$$

In the liquid NH_3 electrolysis, the half-cells reactions are different, such that NH_3 is oxidized into N_2 and NH_4^+ at the anode (equation 9), while the cathode reduces the NH_4^+ into H_2 (equation 10). The combined reaction of the electrolysis for the two cases remains the same, but with different formal potentials, which are 0.059 V and 0.077 V for the aqueous NH_3 splitting and liquid NH_3 splitting, respectively.

$$8NH_3 \rightarrow N_2 + 6NH_4^+ + 6e^- \quad (9)$$

$$6NH_4^+ + 6e^- \rightarrow 3H_2 + 6NH_3 \quad (10)$$

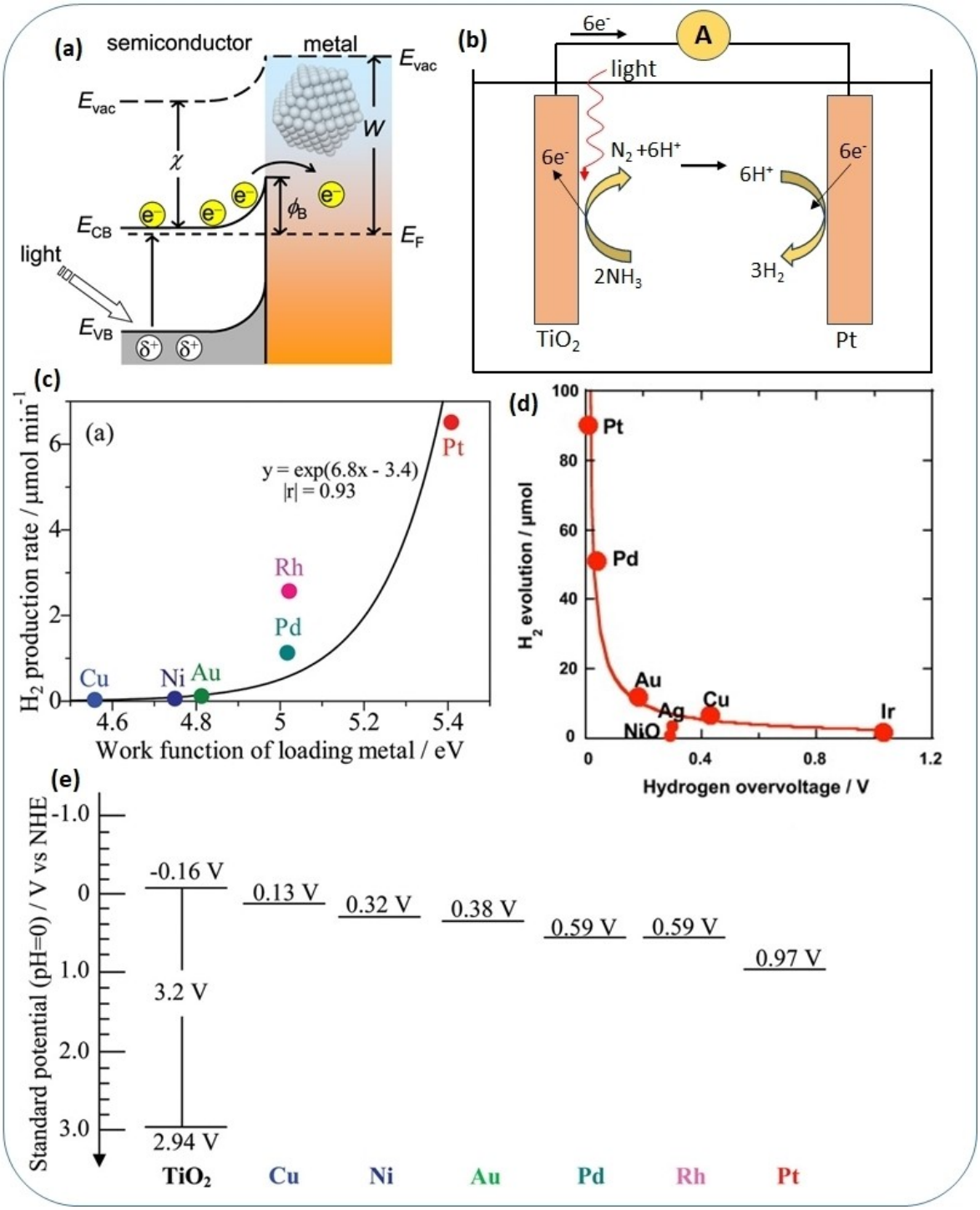

Figure 5. (a) Scheme of semiconductor-metal Schottky junction formation and photoexcited e- and h + generation. Reproduced with permission.[53] Copyright 2020 ACS. (b) Scheme of photofuel cell for NH_3 splitting into N_2 at anode and H_2 at cathode and utilizing TiO_2 as an anode and Pt as a cathode. (c) Variation of H_2 production rate of different metal loading on TiO_2 as a function of workfunction of the metal (Reproduced with permission.[51] Copyright 2012 ACS) and (d) H_2 overpotential. Reproduced with permission.[52] Copyright 2018 RSC. Comparison of standard potentials for valence and conduction bands of TiO_2 and the workfunction of different loading metals. Reproduced with permission.[51] Copyright 2012 ACS.

The advantages of the liquid NH_3 electrolysis over the aqueous NH_3 electrolysis in the alkaline medium were discussed by Little et al.[24] and Hanada et al.,[22] focusing on the overcoming of the electrode surface poisoning, which is a serious problem in aqueous medium. Irrespective of the type of NH_3, the kinetics of the electrode reactions, particularly at the anode, are very sluggish, necessitating the use of electrocatalysts to reduce the overpotential and improve the Faradaic efficiency. Traditionally Pt based electrocatalysts have been extensively investigated[61] for the efficient electrooxidation of NH_3. Differ-

ent approaches were explored, such as change of Pt facet exposure,[62] shape control of Pt nanoparticles,[63] electrochemical roughening of Pt surface[64] and different supports for Pt nanoparticles exposure.[65] These strategies undoubtedly fastened the NH_3 electrooxidation reaction and identified the catalytic reactivity descriptor in Pt-based materials. For instance, studies on different Pt crystal facets revealed that Pt (100) is the most active for NH_3 electrooxidation (Figure 6a), producing ca. 100 times higher oxidation current than Pt (111) and Pt (110). Electrochemical roughening increased the exposed surface area of Pt, which enhanced its mass activity. Because of the very slow kinetics of NH_3 electrooxidation, a very high loading of Pt is required to achieve a fast reaction rate, which is not economical and sustainable, considering the scarcity and high cost of Pt. Moreover, in aqueous medium, Pt particles are easily deactivated by the adsorption of oxygenated species, inhibiting the NH_3 electrooxidation.[66]

To overcome the issue of Pt surface fouling in the aqueous medium, organic solvents were used instead of water. Studies by Peng et al. confirmed the higher stability of Pt nanoparticles in non-aqueous solution, which is attributed to the absence of OH^- adsorption, which otherwise deactivates the Pt-sites.[66] Indeed, Pd nanoparticles revealed even higher NH_3 electrooxidation activity than Pt in the non-aqueous solvent, which otherwise remains inactive in aqueous solvents. In this direction, activity of Pt in the non-aqueous medium was further enhanced by the addition of methanol during the NH_3 electrooxidation.[67] This is evident in the comparison of voltammograms in Figure 6b and chronoamperograms in Figure 6c, showing a smaller onset potential and higher Faradaic current density in the presence of methanol. This effect was attributed to the prevention of nitride formation on the Pt sites, which otherwise poisons the surface, because methanol forms hydrogen bonds with reaction intermediates, weakening the intermediates interaction with the Pt surface. The chemical deactivation of Pt during the NH_3 electrooxidation was recently investigated *in operando* by Kim et al..[68] It was found that NH_3 modifies the electronic structure of Pt and also causes its dissolution, forming a Pt complex, which passivates the electrode surface (Figure 6d). To regain the Pt active sites, NO_x

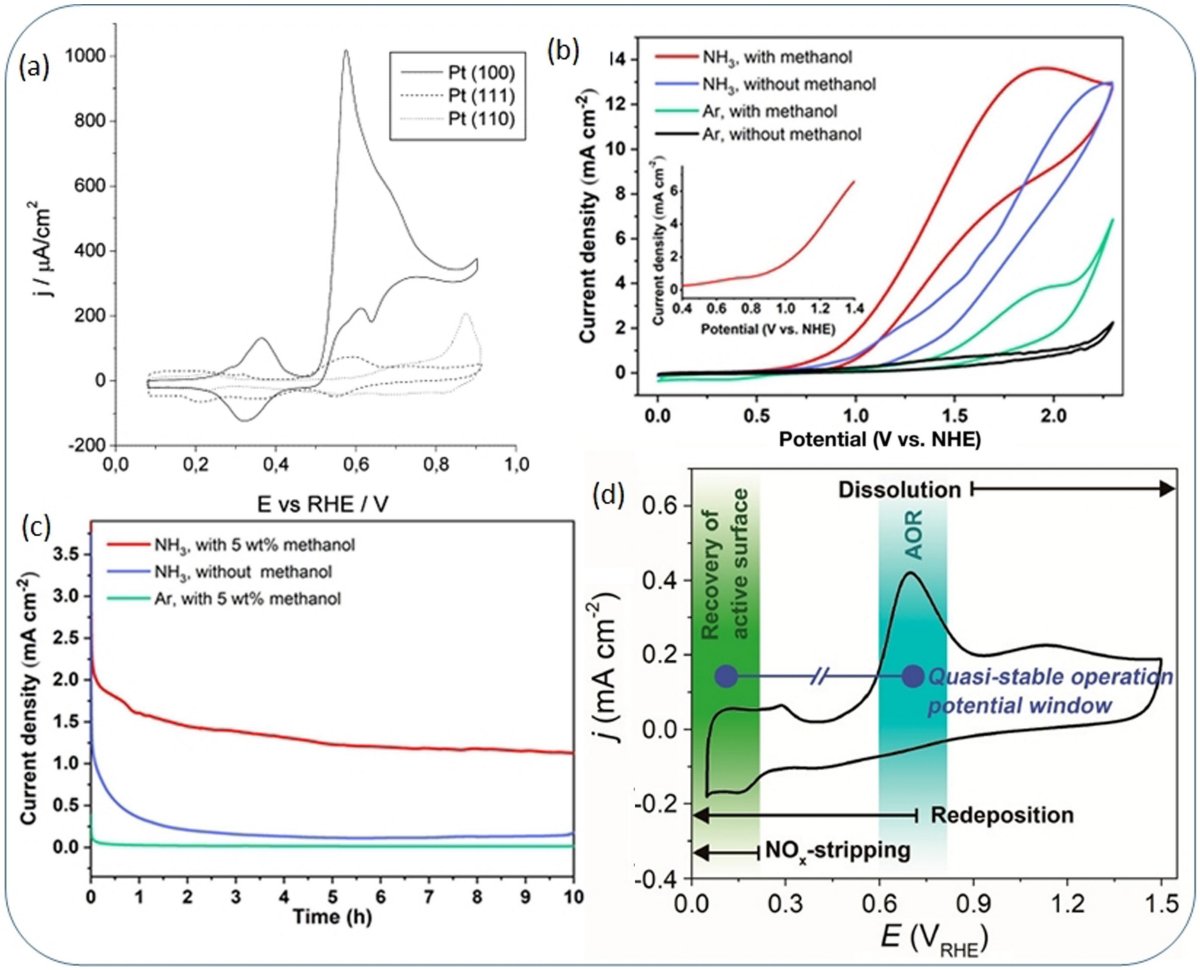

Figure 6. (a) Voltammograms of Pt electrodes with different crystalline orientations in 0.1 M NaOH and 1 mM NH_3 at a scan rate of 50 mV s^{-1}. Reproduced with permission.[62] Copyright 2003 Elsevier. (b) Comparison of CVs of Pt-electrode recorded in argon or ammonia saturated KPF_6-DMF solution in the presence and absence of methanol and (c) amperograms recorded at different methanol percentage in NH_3 and argon saturated KPF_6-DMF solution. Reproduced with permission.[67] Copyright 2022 Elsevier. (d) Voltammogram exhibiting the quasi-stable operation potential window of Pt dissolution/redeposition, and adsorbate removal. Reproduced with permission.[68] Copyright 2020 ACS.

stripping voltammetry should be performed at more negative potential. To lower the Pt loading on the electrode, alloys of Pt have been investigated for the NH_3 electrooxidation. Chan et al. investigated alloys of Pt with different transition metals: Co, Zn, Ni and Fe, dispersed over CNT.[69] The cubic shape of the alloys with small particle sizes in the range of 8 to 11 nm, revealed higher ammonia oxidation current and lower onset potential compared to commercial Pt/C catalyst. Thus, mass and specific activities of Pt are increased upon alloy formation in the NH_3 electrooxidation reaction.

To develop a sustainable electrocatalyst for NH_3 electrooxidation, recent research efforts are focused to develop a Pt-free electrocatalyst. In this endeavor, Huang and coworkers developed a copper oxide-based catalyst, in which a Cu_2O nanowire coated electrode was treated with 500 CV cycles in alkaline aqueous NH_3 solution to *in situ* convert Cu_2O into CuO and generate oxygen vacancies in it.[70] The introduction of oxygen vacancies turned an inactive Cu_2O into a highly active electrocatalyst for NH_3 electrooxidation, evidenced by the emergence of an oxidation wave of high intensity in the oxygen vacancies rich CuO nanowires. Different types of nickel based electrocatalysts have been developed for NH_3 electrooxidation, which activities are compared in a focused review.[60] In a typical work of Xu et al., mixed Ni–Cu hydroxide nanowires were grown over a carbon cloth in hierarchical geometry and investigated for NH_3 electrooxidation.[71] The mixed hydroxide revealed 7-times higher current density than the bare $Ni(OH)_2$ and outperforms the Pt-based electrocatalysts. Huang et al. reported a nanostructured material, Cu_2O wire-in-$Ni(OH)_2$ plate (Figure 7a and 7b), which was passivated by a thin CuO layer, which strongly catalyzed the electrooxidation of NH_3 in alkaline medium, exhibiting high current density (Figure 7c). The high activity of the material was attributed to its unique wire-in-plate nanostructure geometry, providing a synergic effect by the Ni–Cu interaction.[72] Elsewhere, iron nitride was developed as a low cost alternative to catalyze electrooxidation of liquid ammonia, displaying comparable activity as of Pt, but much higher stability than Pt based electrocatalysts.[73]

Besides metal and metal oxides/hydroxides based electrocatalysts, different molecular catalysts based on coordination complexes of transition metals were developed and investigated for their efficiency in NH_3 electrooxidation reaction.[76] In this regard, the recent work by Zott et al. is worth mentioning, reporting an iron complex, iron(II) tris(2-pyridylmethyl)amine (TPA) bis-ammine triflate, $[(TPA)Fe(NH_3)_2]OTf_2$ (Figure 7d).[74] The voltammogram of the materials coated over boron doped diamond electrode reveled an onset potential of 0.7 V (vs. Fc/Fc^+ reference), associated to NH_3 electrooxidation. Moreover, the material was highly stable, as after 50 consecutive CV cycles, a negligible decrease in the oxidation current was noticed (Figure 7e). The high catalytic efficiency of the material was attested by determining the turnover number (TON) of N_2

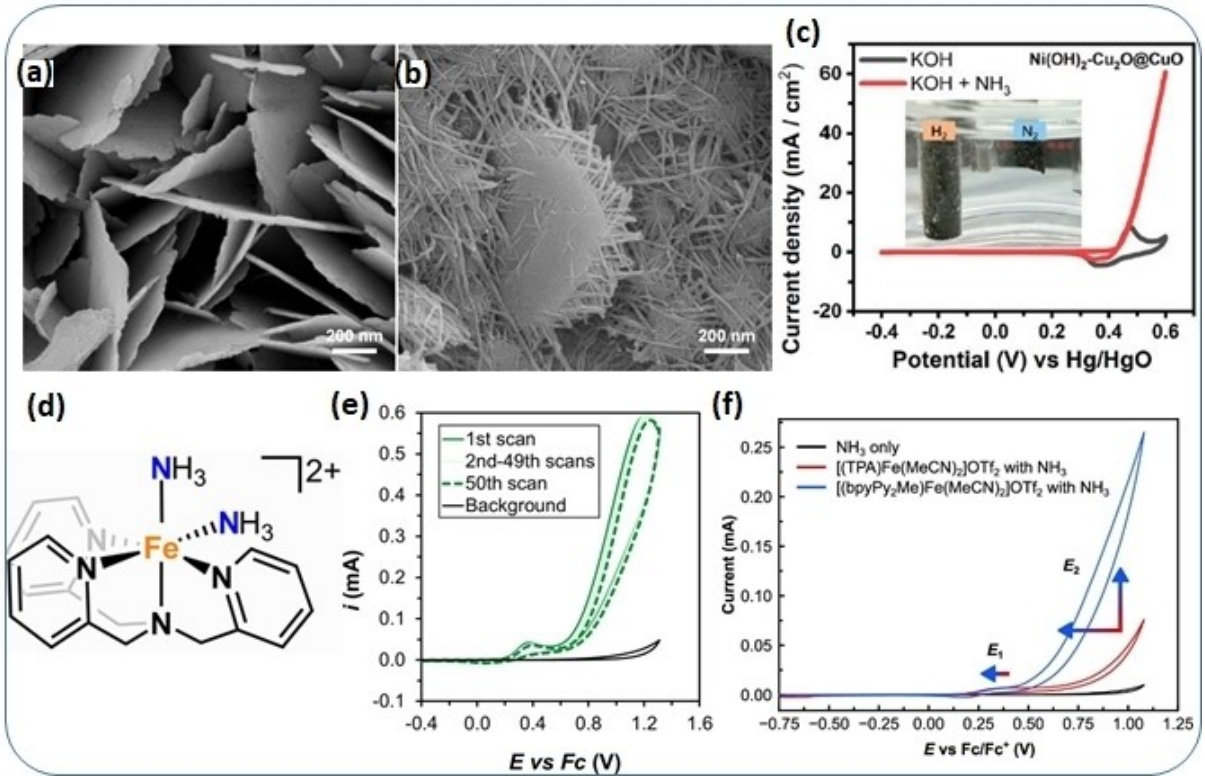

Figure 7. SEM images of (a) $Ni(OH)_2$ nanoplates and (b) $Ni(OH)_2$-Cu_2O@CuO wire-on-plates. (c) Voltammograms of $Ni(OH)_2$-Cu_2O@CuO electrode recorded in 1 M KOH and 1 M KOH + 1 M NH_3. Reproduced with permission.[72] Copyright 2020 ACS. (d) Chemical structure of $[(TPA)Fe(NH_3)_2]OTf_2$ and (e) CV recorded with boron doped diamond electrode in 2.5 mM $[(TPA)Fe(MeCN)_2]OTf_2$ in acetonitrile solution containing 50 mM NH_3 and 50 mM NH_4OTf. Reproduced with permission.[74] Copyright 2019 ACS. (f) Voltammograms of boron doped diamond electrode in acetonitrile containing 0.2 M NH_3 only (black) and with 0.5 mM $[(TPA)Fe(MeCN)_2]OTf_2$ (red) and $[(bpyPy_2Me)Fe(MeCN)_2]OTf_2$. Reproduced with permission.[75] Copyright 2021 ACS.

production as 16, which corresponds to 16 equivalents of N_2 produced by per equivalent of the catalyst.[77] The same group of authors investigated other iron complex by changing the weak-field TPA ligand with strong-field bipyridine ligand, $[(bpyPy_2Me)Fe(MeCN)_2]OTf_2$.[75] Such molecular engineering strongly enhanced the NH_3 electrooxidation, as onset potential shifted to 0.45 V (Figure 7f) and the reaction rate becomes faster by 50 times compared to a $[(TPA)Fe(NH_3)_2]OTf_2$ coated electrode. Additionally, a TON of 149 is recorded, which is the highest reported value for the molecular catalysts. The complex demonstrated excellent structural rigidity, as no demetallation was observed during the catalytic operation, which was attributed to the low spin of Fe(II) state, making the metal center less labile. Besides iron, noble metal Ru-based molecular complexes have been studied for homogeneous as well as heterogeneous electrocatalysis of NH_3[78–81] and some of them revealed TON as high as 125 at room temperature working condition.

3. Fuel Cell Technologies in Ammonia-Based Hydrogen Economy

Fuel cells are considered as a promising technology for clean and efficient power generation and thus are a key technological pillar in the green hydrogen economy.[82–85] Currently, there are almost six types of fuel cells, depending on the type of membrane (electrolyte) used, i.e. alkaline fuel cell (AFC), polymer electrolyte membrane fuel cell (PEMFC), direct methanol fuel cell (DMFC), phosphoric acid fuel cell (PAFC), molten carbonate fuel cell (MCFC) and solid oxide fuel cell (SOFC). The working principle of these fuel cells is similar but the operating temperature ranges, the electrolytes, the fuels used and most importantly their efficiencies are considerably different. Different characteristics of the fuel cells and their potential applications are presented in Table 1. The advantages and disadvantages of fuel cell systems vary depending on their type and are mainly related to their operating temperatures, which has a direct impact on the trends for their respective commercial applications. Low-temperature fuel cells (PEMFC, AFC), for example, are characterized by their rapid start-ups and are therefore competitive in mobile applications. However, they require a highly pure and continuous hydrogen supply, as even small amounts of impurities, such as carbon monoxide (CO) in the fuel can poison the electrode. On the contrary, SOFC and MCFC can operate on fuels containing large fractions of CO, and can thus function either with an external or internal reformer without extensive gas cleaning due to their high operating temperatures.

Among different fuel cells, SOFC typically operates at 600–900 °C and possesses several advantages including high efficiency and fuel flexibility.[86–89] A SOFC consists of a dense, oxygen ion conducting (O^{2-}-SOFC) or proton conducting (H^+-SOFC) solid electrolyte sandwiched between a cathode (oxygen electrode) and an anode (fuel electrode) as depicted in Figure 8. In O^{2-}-SOFCs, oxygen is reduced into oxide ions at the cathode (eq. 11a). The oxide ions then migrate through the electrolyte towards the anode, where they react with the hydrogen to form water vapor (eq. 11b). In an H^+-SOFC on the other hand, hydrogen is oxidized at the anode to form protons (eq. 12a), which migrate through the proton conducting electrolyte towards the cathode, where they react with oxygen to form water (eq. 12b). The overall reaction for both systems is the same (eq. 13).

$$O_2 + 4e^- \rightarrow 2O^{2-} \quad (11a)$$

$$H_2 + O^{2-} \rightarrow H_2O + 2e^- \quad (11b)$$

$$H_2 \rightarrow 2H^+ + 2e^- \quad (12a)$$

$$O_2 + 4H^+ + 4e^- \rightarrow 2H_2O \quad (12b)$$

$$2H_2 + O_2 \rightarrow 2H_2O \quad (13)$$

Table 1. Various types of fuel cells, depending on the electrolyte, operating temperature, fuels, efficiencies and commercial applications.

Types	Electrolyte	Ion through electrolyte	Operating Temperature (°C)	Fuels	Efficiency (%)	Applications
AFC	KOH solution	OH^-	60–80	Pure H_2	60–70	Buses and Spaceships
PEMFC	Polymer membrane (Perfluoro Sulfonic acid)	H^+	50–220	Pure/ reformed H_2	40–60	Vehicles mobile and stationary
DMFC	Polymer membrane (Nafion, sulfonated tetrafluoro ethylene)	H^+	50–120	methanol	40–60	Vehicles mobile and stationary
PAFC	Phosphoric acid	H^+	500–650	Pure/ reformed H_2	55	Stationary
MCFC	Solution of Lithium, Sodium and/ or Potassium	CO_3^{2-}	600–650	Pure/ reformed H_2	55	Stationary and heavy vehicle
O^{2-}-SOFC/ H^+-SOFC	Yttria Stabilized Zirconia (YSZ)/ Y-doped Barium Zirconate	O^{2-}/ H+	600–900/ 400–700	Pure/ reformed H_2, hydrocarbons, biogas, natural gas, ammonia	60–80	Stationary and heavy vehicle

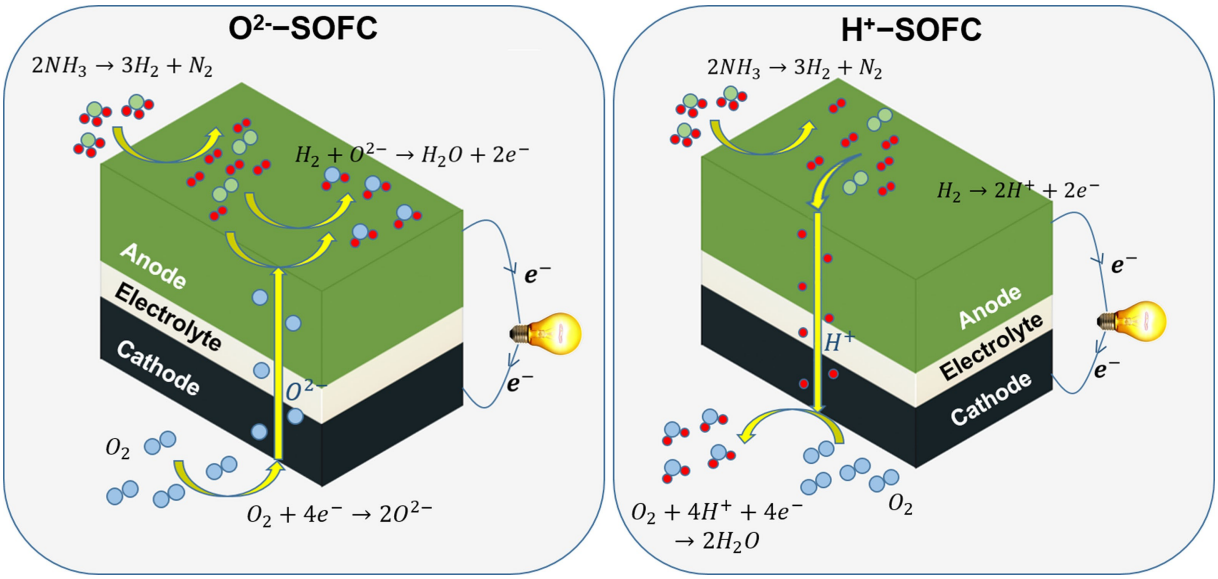

Figure 8. Schematic representation of the SOFC system with oxide ion conducting electrolyte (left) and proton conducting electrolyte (right) including an ammonia decomposition step.

The high operating temperature of SOFCs permits the use of relatively cheap nickel cermet fuel electrodes as well as interconnect materials, and the generated heat in the process can contribute towards accomplishing a high combined heat and power (CHP) efficiency. Although, hydrogen is an ideal fuel in SOFC, but owing to the existing challenges with its production, storage and transportation, its large-scale use is not viable. Alternatively, other fuels, which are a vector of hydrogen, such as hydrocarbons, natural gas, biogas, ethanol, methanol and ammonia can be directly used. There is no need for external reformer or cracker or separation unit with these fuels, as SOFCs are operated at high temperatures. Among the alternative fuels, ammonia has several advantages over the others, as highlighted earlier.

The use of ammonia in SOFC was first described by Farr and Vayenas in 1980.[90] The objective was the production of NO, which they attempted using platinum electrodes on YSZ at temperatures between 900 and 1200 K. Based on the measured open circuit voltage (OCV) and a comparison of the modelled potential-current behavior with experimental data, reaction (14) was assumed to be the dominant one. Reaction (15), in which nitrogen is formed, was specified as a catalytic side reaction.

$$NH_3 + 5O^{2-} \rightarrow 2NO + 3H_2O + 10e^- \quad (14)$$

$$NH_3 + \frac{3}{2}NO \rightarrow \frac{5}{4}N_2 + \frac{3}{2}H_2O \quad (15)$$

Nonetheless, recent studies on direct ammonia fuel cells have clearly highlighted that ammonia decomposes 100% directly into hydrogen and nitrogen in a ratio of 3:1 (as shown in Figure 8) at elevated operation temperatures of SOFC devices, which can be brought down by the use of a catalyst.[91–93] The most active and also most studied catalyst for NH_3 decomposition is ruthenium (Ru). However, Ru is scarce and therefore expensive. An alternative to Ru is nickel (Ni), as it also performs well and is less expensive. The work of Wojcik et al. showed the feasibility of *in situ* utilization of ammonia in SOFC using Fe-based catalysts in a tubular fuel cell with a silver electrode to combine catalytic cracking and SOFC in one process.[94] The performance of the silver electrode without Fe-catalyst was significantly lower with NH_3 than with H_2 as fuel. The Fe-catalyst increased the performance of the fuel cell with NH_3 fuel to almost the same level as that of the H_2 fuel. The comparison with a platinum electrode without Fe-catalyst also showed very similar performance for NH_3 and H_2 fuel. Fournier et al. compared the NH_3 conversion of Pt, Ag and NiO/YSZ, and showed that the conversion on NiO/YSZ is twice as high as on Pt or Ag.[95] At 1073 K, the conversion of NH_3 on NiO/YSZ is above 90%. However, the product gas composition analysis was not carried out to determine the production of NO. Ma et al. performed the thermodynamic analysis and found that the NO partial pressure increases with the ammonia conversion rate and with increasing temperature, although the absolute amounts of NO are negligibly small.[93] However, in real NH_3 fed SOFC operation with Ni-based electrodes, NO was not detectable in the output gas stream with a gas chromatographic analysis. This confirms that ammonia is decomposed completely in-situ into N_2 and H_2 at elevated temperature. At low temperatures, NH_3 needs to be cracked in a separate reactor providing the necessary temperatures and catalysts.

Since ammonia is decomposed into hydrogen and nitrogen, the direct ammonia SOFC works like a standard hydrogen fuel cell (Figure 8). The nitrogen merely dilutes the reactant, which can lead to a slight reduction of the SOFC performance. However, this is significant only when the fuel conversion rate is high. Compared to the O^{2-}-SOFC, the H^+-SOFC has some additional advantages when using ammonia as a fuel. Indeed,

the steam is produced at the cathode and therefore does not humidify any remaining ammonia traces in the output gas, which could corrode steel tubes or interconnects in the system. The cell materials of both SOFCs are also suitable to perform the electrolysis reaction by reversing the current and changing the feed gas. Thus, the same system can be used to use and produce electrical current.

3.1. High Temperature Direct NH_3 Fed O^{2-}-SOFC

As already mentioned, O^{2-}-SOFC consists of mainly three components i.e. electrolyte, cathode and anode. The state-of-the-art electrolyte material is 8 mol% yttria-stabilized zirconia (8YSZ) for SOFC due to its excellent mechanical strength and stability as well as its considerable ionic conductivity at elevated temperatures (800-1000 °C).[96,97] Some other electrolytes are gadolinium or scandium doped ceria ($Ce_{0.8}Gd_{0.2}O_{2-\delta}$, GDC or $Ce_{0.8}Sm_{0.2}O_{2-\delta}$, SDC) and lanthanum strontium magnesium gallates (LSGM), however the use of ceria based materials is limited due to their redox instability, resulting in electronic conductivity under reducing atmosphere and at high operating temperature.[98–101] More details about SOFC electrolytes have been discussed in detail in other reports.[102–106] With regard to the oxygen electrode of SOFCs, lanthanum- and strontium-based perovskites e.g. (La, Sr)(Co, Fe)$O_{3-\delta}$, (LSCF), (La, Sr)$CoO_{3-\delta}$ (LSC) and (La, Sr)MnO_3 (LSM) mixed with YSZ (LSM + YSZ) are considered as suitable materials due to their high mixed ionic electronic conductivity.[107–112] Recently, some other perovskites, double perovskites, and Ruddlesden–Popper (RP) structures have also shown promise as cathode materials.[113–121] Further details about SOFC cathodes have been discussed in detail in other reviews.[122–124] The most important component of direct ammonia SOFCs is the anode, as all the rate-determining electrocatalytic reactions take place at the anode. For a high-performance direct ammonia SOFC, the ideal anode has the following requirements: a) excellent catalytic activity to ensure a complete NH_3 decomposition before reaching the triple-phase boundaries (TPB) of the electrode, b) adequate porosity to ensure easy diffusion of gases like NH_3, H_2, N_2, steam, and c) considerable ionic and electronic conductivity or mixed conductivity, thus increasing the TPB and improving the overall kinetics of the cells. In the next section, the properties and performance of various anode materials in direct ammonia O^{2-}-SOFC operation are discussed in detail.

Anode electro-catalysts materials: The direct ammonia fueled SOFCs utilizes the hydrogen produced by decomposition of ammonia at the fuel electrode (anode), so a high ammonia decomposition activity is crucial for the anode materials. Therefore, it is important for a high-performance NH_3 fuel cell to select active electro-catalyst materials with high selectivity for N_2 as the only nitrogen product and to avoid the formation of NO_x during the oxidation of NH_3. So far, state-of-the-art anode materials of SOFC containing Ni-catalyst cermets (Ni-YSZ or Ni/doped ceria) have been extensively studied, due to their high catalytic activity, selectivity and cost-effectiveness as well as extremely high ammonia conversion rates above 600 °C.[125] As stated by thermodynamics, the NH_3 can be decomposed in the absence of catalyst, however, the reaction rate will be much slower in comparison to the presence of catalysts.[126,127] Ma et al.[93] investigated the single cell consisting of a Ni-$Ce_{0.8}Sm_{0.2}O_{1.9}$ (SDC) anode, SDC electrolyte and an $Sm_{0.5}Sr_{0.5}CoO_{3-\delta}$ (SSC)-SDC cathode under ammonia as a fuel gas and compared the performance under pure ammonia and hydrogen as a fuel gas. Compared to ammonia, slightly higher OCVs and cell performance were observed with hydrogen as fuel. For instance, maximum power densities of 168.1 and 191.8 $mW \cdot cm^{-2}$ were achieved at 600 °C with ammonia and hydrogen as the fuels, respectively (Figure 9a). This suggests that ammonia is a suitable alternative of hydrogen. In addition, the polarization resistance (R_p) as well as the ohmic resistance (R_s) were slightly higher with ammonia compared to hydrogen as fuel. At 600 °C, for example, R_p values of 0.52 and 0.39 $\Omega \cdot cm^2$ were observed under ammonia and hydrogen as fuels, respectively. The ohmic resistances were also slightly higher for ammonia (1 $\Omega \cdot cm^2$) in comparison to hydrogen (0.95 $\Omega \cdot cm^2$) (Figure 9b). Furthermore, a gas chromatography analysis of the anode exhaust gas revealed no traces of NO. The ammonia was

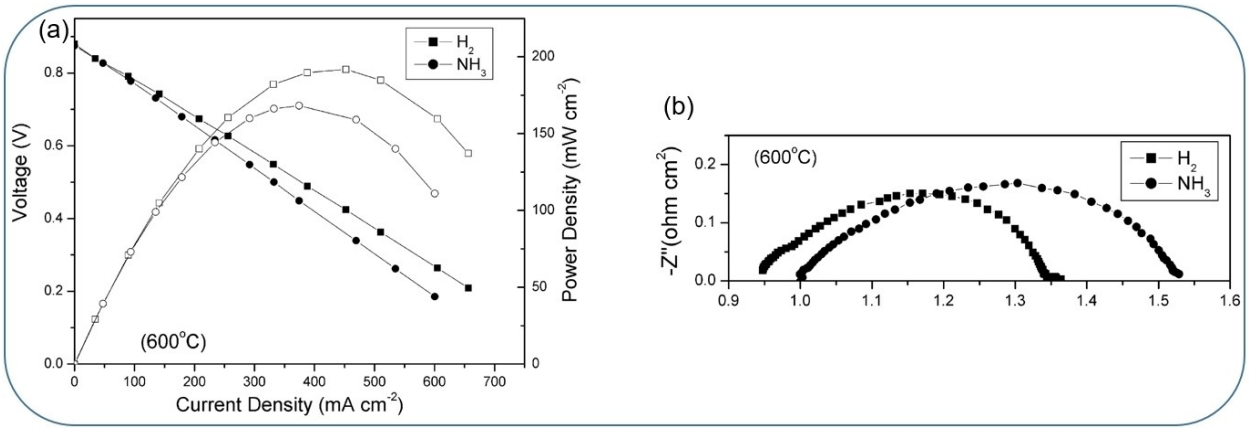

Figure 9. (a) Comparison of I–V–P curves, and (b) comparison of impedance spectra of single cell with hydrogen and ammonia fuels at OCV and 600 °C. Reproduced with permission.[93] Copyright 2006, Elsevier.

completely decomposed into hydrogen and nitrogen at 600 and 700 °C, however at 500 °C it was not fully cracked. At 500 °C, 21% and 5% NH_3 were detected in the exhaust gas with an ammonia gas flow of 30 and 5 $ml \cdot min^{-1}$, respectively.

In another work, Xu et al.[128] investigated the performance of single cell containing a Ni-YSZ fuel electrode with a surface coating of $CeO_{2-\delta}$ nanoparticles under ammonia and hydrogen as fuel gas in 700–800 °C temperature range. In case of the bare Ni-YSZ electrode, a maximum power density of 1.59 and 1.37 $W \cdot cm^{-2}$ at 800 °C was observed for hydrogen and ammonia as fuels (Figure 10a). The decrease in OCV value was also observed when ammonia was used instead of hydrogen, which is attributed to the relatively lower partial pressure of hydrogen under ammonia. Moreover, a lower R_p was observed when the single cell was fueled with hydrogen (0.239 $\Omega \cdot cm^2$ at 800 °C) in comparison to ammonia (0.323 $\Omega \cdot cm^2$ at 800 °C). When the Ni-YSZ electrode was coated with $CeO_{2-\delta}$ nanoparticles, the cell exhibited a higher performance for both H_2 and NH_3 fuels. However, again a lower performance was observed with ammonia (1.89 $W \cdot cm^{-2}$ at 800 °C) in comparison to hydrogen fuel (2.14 $W \cdot cm^{-2}$ at 800 °C) (Figure 10c). Interestingly, in the case of a $CeO_{2-\delta}$ infiltrated Ni-YSZ electrode, the cell showed similar R_p and R_s with both H_2 and ammonia fuels at 800 °C (Figure 10b and 10d), which could be due to improved mass/charge transfer kinetics and higher activity towards NH_3 decomposition.

The distribution of relaxation times (DRT) analyses of impedance spectra of single cell under hydrogen and ammonia fuels revealed five distinct peaks (Figure 10e) for the bare Ni-YSZ electrode. The main difference in bare electrode and $CeO_{2-\delta}$ coated one is observed for P2 peak. The $CeO_{2-\delta}$ coated electrode shows a smaller P2 peak, which indicates faster NH_3 adsorption, decomposition, and/or H_2 dissociation. Moreover, the DRT curves recorded on single cells with $CeO_{2-\delta}$ infiltration show negligible difference for H_2 and ammonia fuels at 800 °C (Figure 10f), indicating that the $CeO_{2-\delta}$ infiltrated electrode has higher activity for ammonia decomposition. The performance of single cell containing bulk Ni-YSZ, thin film Ni-YSZ (TF–Ni/YSZ) active layer and thin film Ni-GDC (TF–Ni/GDC) as fuel electrodes as well as an LSC oxygen electrode with thin GDC barrier layer, were compared under H_2 and ammonia fuels in the temperature range of 500–650 °C by Oh et al.[129] The lower OCV was observed for ammonia compared to H_2 for all temperatures. In addition, the ammonia decomposition was also similar for all

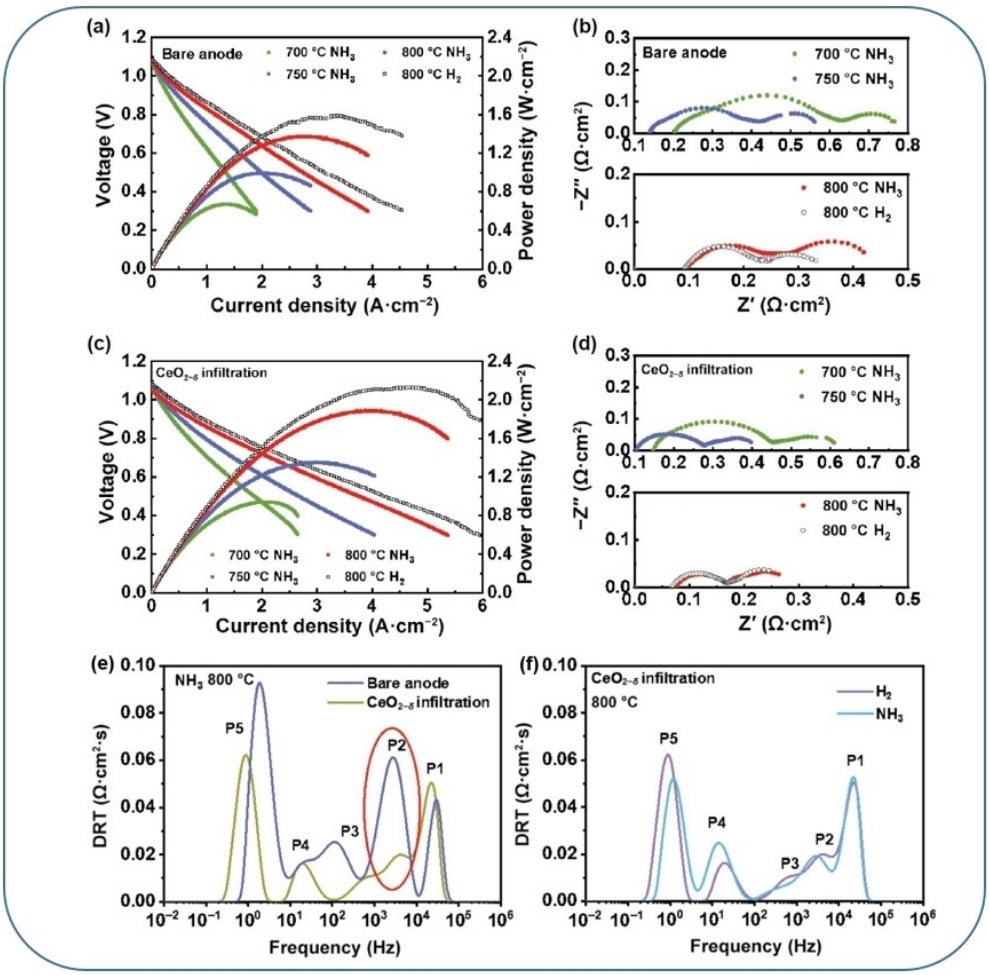

Figure 10. Comparison of I–V–P curves (a, c), impedance spectra (b, d), and DRT plots at 800 °C (e, f) of single cells with hydrogen and ammonia fuels. Reproduced with permission.[128] Copyright 2022, Springer Nature.

the cells, however, the extent of ammonia decomposition was decreased with reducing temperature from 650 to 500 °C. The performance of the TF–Ni/GDC electrode containing single cell was the highest among all for both H_2 and ammonia fuels. For instance, at 600 °C the peak power densities were 394, 1244, 1587 $mW \cdot cm^{-2}$ under hydrogen and 344, 911, 557 $mW \cdot cm^{-2}$ with ammonia fuels for the single cells containing Ni/YSZ, TF–Ni/YSZ and TF–Ni/GDC electrodes, respectively (Figure 11). The total resistance of the cell increased from 3.48 to 4.02 $\Omega \cdot cm^2$ at 550 °C with ammonia compared to that of hydrogen for Ni-YSZ cell. In addition, the R_s also increased by 0.028 $\Omega \cdot cm^2$ mainly due to the endothermic ammonia decomposition reaction. The increase in R_p is mainly observed at the low frequencies and is generally attributed to the gas diffusion of the reactants. Similar behavior was observed for TF–Ni/YSZ and TF–Ni/GDC cell, the total resistance increased from 0.378 to 0.807 $\Omega \cdot cm^2$ for the TF–Ni/YSZ cell and from 0.193 to 0.775 $\Omega \cdot cm^2$ for the TF–Ni/GDC cell at 550 °C with ammonia compared to that of hydrogen.

The above result proves that Ni/YSZ is an efficient catalyst for ammonia decomposition above 700 °C, however its catalytic activity decreases rapidly at lower temperatures. Therefore, the catalysts must be modified if they are to be used at lower temperatures (≤700 °C). In this context, Wang et al. modified the Ni/YSZ by adding barium to the cermet electrode (Ni, 30% and Ba, 15%)[130] and found that this addition significantly improved the performance of the cell by weakening the hydrogen poisoning effect of ammonia decomposition. The effect of the addition of different transition metals i.e. Ni, Co and Fe in $Ce_{0.8}Sm_{0.2}O_{2-\delta}$ (SDC) cermet electrodes were investigated by Akimoto et al.[131] and it was found that Ni/SDC has a high activity for hydrogen, but not for ammonia. The performance of Co/SDC was poor, while Fe/SDC has the highest activity for ammonia among three transition metals in 700–900 °C temperature range. Moreover, remarkably, the anode made of Ni–Fe alloy/SDC (Ni:Fe, 40:60) showed the best performance among all.

In addition to the cermet electrode, some perovskite anodes infiltrated with transition metals are gaining attention for direct ammonia fueled SOFCs. For example, the electrolyte supported single cell with NiCo/LST ($La_{0.55}Sr_{0.3}TiO_{3-\delta}$) infiltrated $Sm_{0.2}Ce_{0.8}O_{1.9}$ (SDC) anode, SDC electrolyte and BSCF or SSC ($Sm_{0.5}Sr_{0.5}CoO_{3-\delta}$) cathode delivered the maximum power density of 361 $mW \cdot cm^{-2}$ at 800 °C using NH_3 fuel.[132] The performance of this cell was significantly higher than single Ni or Co infiltrated LST anode. Sorcar et al. prepared the electrolyte supported single cells with YSZ electrolyte, a 5%Cu/$LaTiO_2N$ (lanthanum titanium oxynitride) cermet with GDC ($Ce_{0.9}Gd_{0.1}O_{1.95}$) anode infiltrated with an alloy of NiFe nanoparticles, and LSCF + GDC/LSCF cathode and investigated their performance in direct ammonia SOFC.[133] A maximum power density of 228 $mW \cdot cm^{-2}$ was obtained at 750 °C.

The results so far have demonstrated the promising behavior of the SOFC when ammonia is used directly as a fuel with small button cells. However, with regard to scalability and industrial applications, it is also essential to investigate the behavior of a large single cell under the same conditions. In this context, Cinti et al.,[134] investigated the performance behavior of a large anode supported single cell (active area, 50 cm^2) with Ni/YSZ anode, YSZ electrolyte and LSCF oxygen electrode with GDC barrier layer, under ammonia, hydrogen/nitrogen mixture of 3:1 (simulated ammonia) and pure hydrogen. A maximum

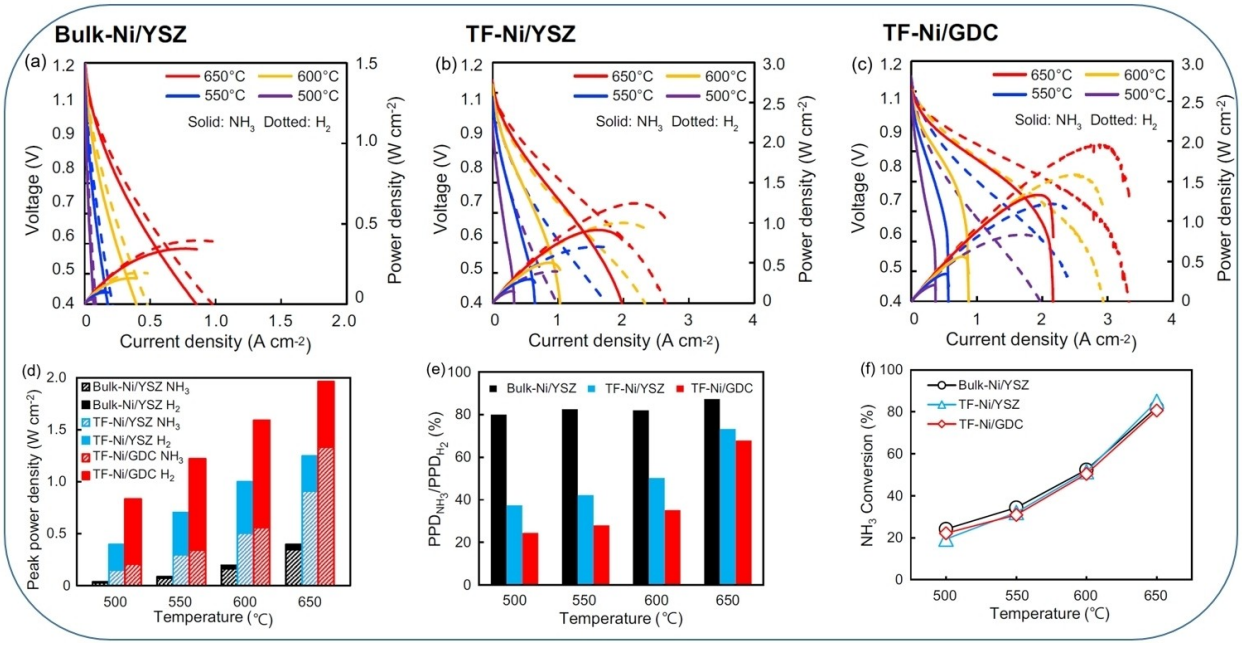

Figure 11. (a, b, c) Comparison of I–V–P curves for single cells containing bulk-Ni/YSZ, TF–Ni/YSZ, and TF–Ni/GDC with hydrogen (dotted line) or ammonia (solid line) fuel; (d) Comparison of the peak power density of each single cell with hydrogen (filled) or ammonia (slashed) fuel, (e) Comparison of peak power density ratio, PPD_{NH3}/PPD_{H2} (%), and (f) Fuel conversion of NH_3 measured by collecting unconverted ammonia at the exhaust of each single cell at OCV. Reproduced with permission.[129] Copyright 2022, Elsevier.

power density of 0.3 $W \cdot cm^{-2}$ at 800 °C was achieved with the efficiency of 18%, fuel utilization of 33% using the flow of 7.13 $ml \cdot min^{-1} \cdot cm^{-2}$ of ammonia. The efficiency and the fuel utilization increased up to 30% and 55%, respectively, with the reduction of ammonia flow rate. With decreasing the operating temperature, the cracking reaction of ammonia shifts from outside of the cell to the active area of the cell, demonstrated by the internal cell cooling for the temperature below 800 °C.

Hagen et al.[135] compared the performance of a large Ni/YSZ anode supported single cells (53×53 mm^2 with active area of 16 cm^2) under direct ammonia and under hydrogen nitrogen mixture (simulated ammonia) in the ratio of 3:1 at 850 °C. Interestingly, the performance of the cell was the same under both conditions (maximum power density ~0.9 $W \cdot cm^{-2}$, Figure 12a), which verifies that ammonia is fully cracked in the SOFC at 850 °C. Moreover, the long-term stability test up to 1500 h at 1 $A \cdot cm^{-2}$ and 850 °C under direct ammonia as a fuel showed similar degradation rate of ca. 2–4%/1000 h as that of hydrogen as fuel (Figure 12b). Furthermore, the formation of toxic NO_x was not detected with ammonia fuel. The performance of different O^{2-}-SOFC single cells with direct ammonia and hydrogen as fuel is summarized in Table 2.

As a summary for direct O^{2-}-SOFC, the state-of-the-art Ni-YSZ anode as well as some recently developed anode materials, showed promising behavior and exhibited complete dissociation of ammonia at elevated temperature above 700 °C, and furthermore no NO_x formation has been detected so far. In general, the performance behavior of the single cells shows a slightly lower performance with ammonia than hydrogen as fuel, which is mainly due to the endothermic ammonia decomposition, dilution effect of the fuel with nitrogen and the hydrogen poisoning effect. The ohmic and polarization resistances are also slightly higher under ammonia fuel than with pure hydrogen. Moreover, the single cells show similar performance and degradation behavior with direct ammonia and simulated ammonia as fuel, especially at higher operating temperatures ~800 °C or above. In addition, the performance of single cells is found to be the same for ammonia and hydrogen as fuel with very active catalysts.

3.2. High Temperature NH_3 Fed H^+-SOFC

Similar to O^{2-}-SOFC, the H^+-SOFC comprises three main components, which are electrolyte, cathode and anode. The conventional electrolyte materials for H^+-SOFC are yttrium doped $BaZrO_3$ (BZY), $BaCeO_3$ (BCY) or their solid solutions Ba(Ce, Zr)O_3 (BCZY).[136–141] Ce-rich electrolytes generally show high proton conductivity but are chemically less stable especially under steam atmosphere.[139,142] On the other hand, Zr-rich electrolytes are chemically more stable especially under steam containing atmosphere but suffer from low sinter ability. As a result, a comparatively higher sintering temperature above 1600 °C, is required.[142] To further improve the chemical stability under steam atmosphere, the BCZY electrolyte was co-doped with Yb, which also allows higher Ce-content in the structure. In this respect, the electrolyte materials $BaCe_{0.7}Zr_{0.1}Y_{0.1}Yb_{0.1}O_{3-\delta}$ (BCZYYb7111) and $BaCe_{0.4}Zr_{0.4}Y_{0.1}Yb_{0.1}O_{3-\delta}$ (BCZYYb4411) have shown a simultaneously improved proton conductivity and chemical stability.[143–145]

With regard to the cathode of H^+-SOFCs, the state-of-the-art materials are mixed ionic and electronic conductors ($O^{2-}/H^+/e^-$) such as barium- and strontium- based perovskites e.g. (Ba, Sr)(Co, Fe)$O_{3-\delta}$,[146] double perovskites $PrBaCo_2O_{5+\delta}$,[147] $PrBa_{0.5}Sr_{0.5}Co_2O_{5+\delta}$[144] and Ruddlesden Popper nickelates ($Ln_2NiO_{4+\delta}$, Ln=La, Pr or Nd).[148,149] The corresponding cells have shown promising performance under H^+-SOFC conditions using hydrogen as fuel and further details can be seen in some recent review reports.[150,151]

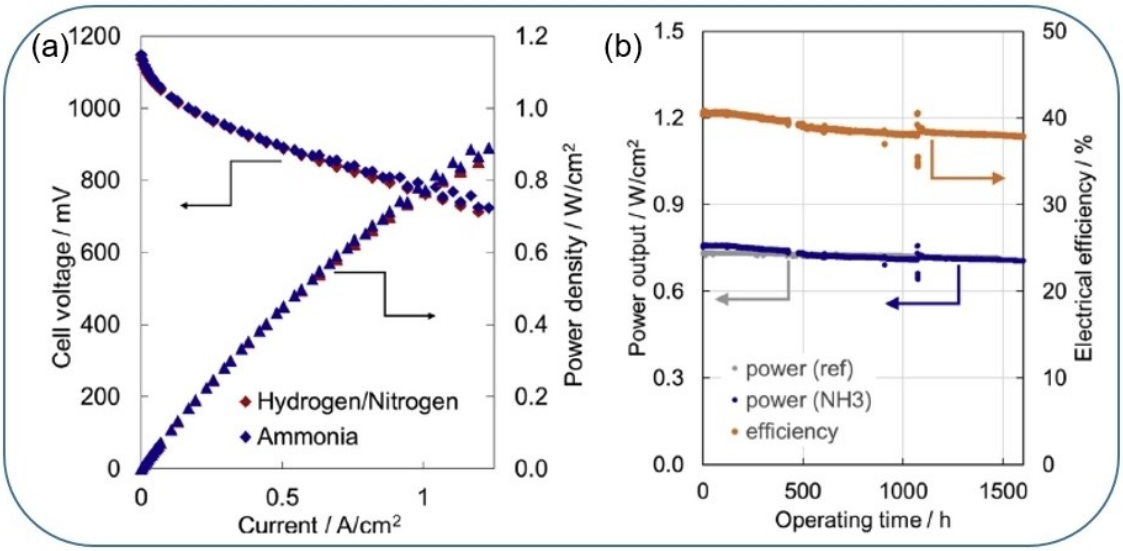

Figure 12. (a) Comparison of I–V–P curves of single cell at 850 °C with the ammonia and corresponding hydrogen/nitrogen mixture (3/1 ratio), and (b) power output (blue curve) and electrical efficiency (orange curve) under current load of 1 $A.cm^{-2}$ up to 1000 h at 850 °C. Reproduced with permission.[135] Copyright 2019, Elsevier.

Table 2. Performance of single cells under direct ammonia and hydrogen as fuel for O^{2-}-SOFC.

Single cell	Electrolyte thickness (μm)	T (°C)	Peak power density (mW.cm^{-2})		ref
			Ammonia fuel	H_2 fuel	
Ni-SDC//SDC//$Sm_{0.5}Sr_{0.5}CoO_{3-\delta}$ (SSC)	50	700	253	271	93
		600	168	192	
		500	65	82	
Ni-YSZ//YSZ//GDC//LSCF-GDC	6	650	344	394	129
		600	161	159	
TF Ni-YSZ//YSZ//GDC//LSC	1	650	911	1244	129
		600	502	1000	
TF Ni-GDC//YSZ//GDC//LSC	1	650	1330	1961	129
		600	557	1587	
Ni-YSZ//YSZ//GDC//PBCC ($PrBa_{0.8}Ca_{0.2}Co_2O_{6-\delta}$)	8	800	1375	1594	128
		750	997	–	
		700	673	–	
$CeO_{2-\delta}$ infil. Ni-YSZ//YSZ//GDC//PBCC	8	800	1893	2144	128
		750	1351	–	
		700	941	–	
NiO-SDC//SDC//BSCF	10	650	1190	1872	163
		600	434	1357	
		550	167	748	
PSCF//SDC//BCFZY (PSCF: $Pr_{0.6}Sr_{0.4}Co_{0.2}Fe_{0.8}O_{3-\delta}$ BCFZY: $BaCo_{0.4}Fe_{0.4}Zr_{0.1}Y_{0.1}O_{3-\delta}$)	400	800	288	395	164
		750	207	318	
		700	139	225	
		650	86	160	
Ru-PSCF//SDC//BCFZY (Ru-PSCF: $Pr_{0.6}Sr_{0.4}Co_{0.2}Fe_{0.75}Ru_{0.05}O_{3-\delta}$ BCFZY: $BaCo_{0.4}Fe_{0.4}Zr_{0.1}Y_{0.1}O_{3-\delta}$)	400	800	483	512	164
		750	381	401	
		700	280	302	
		650	183	207	
NiCo-LST/SDC//SDC//BSCF	350	800	361	479	132
		750	260	393	
		700	190	305	
		650	120	218	
Ni-YSZ//YSZ//GDC//LSCF	10	750	536 at 0.7 V	–	165
Ni-Fe-SDC//LSGM//SSC	500	900	~400	–	131
		800	~280	–	
		700	~200	–	
Ni-YSZ//YSZ//LSM ($La_{0.5}Sr_{0.5}MnO_3$)	30	850	526	–	96
		750	~300	–	
		650	~100	–	
Ni-BCNO//BCNO//LSCO (BCNO: $BaCe_{0.9}Nd_{0.1}O_{3-\delta}$ LSCO: $La_{0.5}Sr_{0.5}CoO_{3-\delta}$)	20	700	315	335	166
Ni-BCGO//BCNO//LSCO-BCGO (BCGO: $BaCe_{0.8}Gd_{0.2}O_{2.9}$ LSCO: $La_{0.5}Sr_{0.5}CoO_{3-\delta}$)	50	750	384	–	167
		700	355	–	
		650	184	–	
		600	96	–	
Ni-YSZ//YSZ//PZO-60YSZ (PZO: $Pr_2Zr_2O_7$)	10	800	1220	1220	168
		700	760	–	
		600	250	280	
Ni-YSZ/YSZ/LSC-GDC	3	850	1174	1192	169

Table 2. continued

Single cell	Electrolyte thickness (μm)	T (°C)	Peak power density (mW.cm^{-2})		ref
			Ammonia fuel	H_2 fuel	
		800	1078	1104	
		850	1202 (at 3 atm)	1235 (at 3 atm)	
		800	1148 (at 3 atm)	1193 (at 3 atm)	
Ni-YSZ/Ni-SSZ//SSZ//SSZ-LSM	20	800	1028	1204	170
		750	654	741	
		700	451	462	
		650	266	292	

Like O^{2-}-SOFC, the anode is the most critical component of the direct ammonia H^+-SOFC, as the ammonia decomposition as well as all rate-determining electrocatalytic reactions take place there. The anode for direct ammonia SOFC should possess a) an excellent catalytic activity for NH_3 decomposition to ensure complete decomposition, b) an adequate ionic and electronic conductivity or mixed conductivity, thus increasing the TPB and improving the overall kinetics of the cells as well as hydrogen oxidation reaction, c) an adequate porosity for diffusion and distribution of gases like NH_3, H_2, N_2, steam, and d) it should be chemically stable under reducing atmosphere. In this respect, Ni-based cermets (ceramic-metal composites) are widely used due to their high catalytic activity and cost-effectiveness.[151] Ni-cermets generally consist of Ni and a proton conducting phase same as electrolyte to enhance the chemical and mechanical compatibility between anode and electrolyte. Some widely used anodes for H^+-SOFCs are Ni-$BaZr_{0.8}Y_{0.2}O_{3-\delta}$,[152] Ni-$BaZr_{0.85}Y_{0.15}O_{3-\delta}$,[153] Ni-$BaCe_{0.2}Zr_{0.7}Y_{0.1}O_{3-\delta}$,[154] Ni-$BaCe_{0.55}Zr_{0.3}Y_{0.15}O_{3-\delta}$,[155] Ni-$BaCe_{0.7}Zr_{0.1}Yb_{0.1}Y_{0.1}O_{3-\delta}$.[156] The performance of various anode materials in direct ammonia H^+-SOFC operation are discussed in detail in the next section.

Anode electro-catalysts materials: Just like the O^{2-}-SOFC, the H^+-SOFC requires a highly active catalyst for decomposition of ammonia as well as oxidation of hydrogen, especially at a relatively low operating temperature range of 500–700 °C. It is important to note that the performance of ammonia fueled SOFCs decreases at lower temperatures owing to insufficient ammonia decomposition activity of conventional fuel electrodes. Some Ni containing anodes such as Ni-Ba(Zr, Y)$O_{3-\delta}$ (Ni/BZY),[157] Ni-$BaCe_{0.75}Y_{0.25}O_{3-\delta}$ (Ni/BCY),[158] Ni-$BaCe_{0.4}Zr_{0.4}Y_{0.2}O_{3-\delta}$ (Ni/BCZY)[92] have been investigated under H^+−SOFC conditions with direct ammonia as fuel. Jang et al. compared the catalytic activity in two step utilization mechanism of ammonia for Ni/YSZ, Ni/gadolinium-doped ceria (Ni/GDC) and Ni/$BaCe_{0.75}Y_{0.25}O_{3-\delta}$ (Ni/BCY25), and found that Ni/BCY showed the highest activity for ammonia decomposition and SOFC single cell performance with ammonia fuel in 500–700 °C temperature range.[159] The poisoning effect of water and hydrogen on ammonia decomposition over Ni/BCY25 was also evaluated and it was found that the ammonia conversion is significantly reduced even with a small amount of water (0.8%). The ammonia conversion was dropped sharply from 98.6% to 55.0%, mainly due to dissociative adsorption of water on the surface of Ni/BCY25. Consequently, the active reaction sites may be occupied by the species such as protons and hydroxide groups. The performance of electrolyte supported single cells was investigated under both hydrogen and ammonia containing fuels (Figure 13a) and it was found that the performance of the single cell was lower with ammonia containing fuels than hydrogen. This effect was more pronounced at lower temperatures, which is mainly due to the lower activity of ammonia decomposition at lower temperatures. The investigation of cell performance at different water contents showed no negative effects (Figure 13b), rather the ohmic resistance or the total

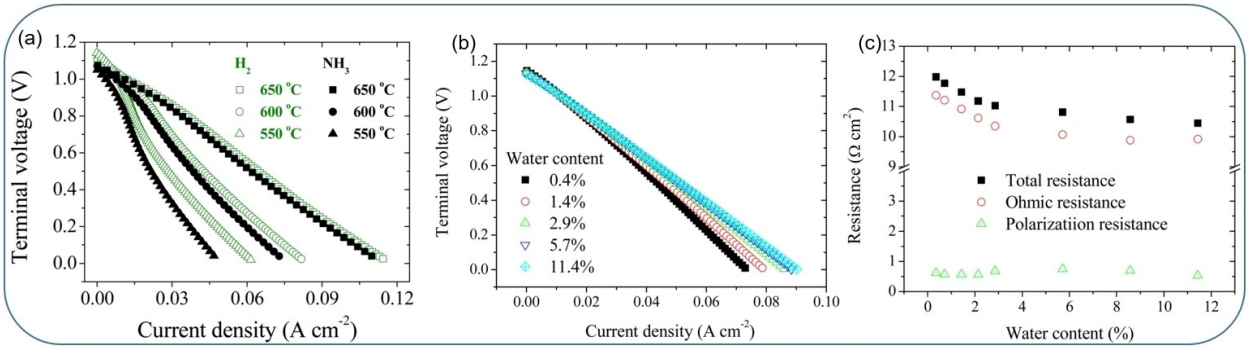

Figure 13. (a) I–V curves of electrolyte supported Ni/BCY25//BCY10//Pt single cell under hydrogen and ammonia fuels, (b) I–V curves with different steam content at 600 °C, and (c) the variation of total, ohmic and polarization resistances as a function of steam content at 600 °C. Reprinted with permission from.[159] Copyright 2015, American Chemical Society.

resistance was reduced with increasing water content (Figure 13c). It was concluded that the water poisoning does not affect the cell performance.

The activity of ammonia decomposition and the performance of single cells containing Ni–$Ba(Zr,Y)O_{3-\delta}$ (Ni/BZY) fuel electrode were also investigated.[157] The catalytic decomposition of ammonia revealed that the ammonia was completely decomposed at ~600 °C. Moreover, Ni/BZY10 (10% Y doped BZY) showed higher activity for ammonia decomposition than Ni/BCY10 (10% Y doped BCY). In addition, Ni/BZY20 (20% Y doped BZY) displayed higher catalytic activity than Ni/BZY10, mainly due to the higher basicity of BZY and higher resistance to the hydrogen poisoning effect. The electrochemical performance of an anode supported single cells (Ni/BZY20//BZY20//Pt) under ammonia and hydrogen containing fuels were compared in the 600–700 °C temperature range. The OCV of the cell was lower in ammonia containing fuels than under hydrogen, also it was lower than the theoretical OCV in both cases. The lower OCV was mainly due to the hole conduction i.e., electronic leakage through the BZY20 electrolyte. The performance of the cell was lower in ammonia containing fuels than with hydrogen. The ammonia conversion was also estimated from OCV and the ammonia conversion was ca. 70% at 600 °C, although it was completely decomposed during catalytic activity test at 600 °C. This is mainly because the porosity in the electrode structure was significantly lower than the one used for the catalytic activity test. Therefore, higher temperatures are required and/or the anode microstructure should be modified so that a long contact time of the fuel gas with the electrode is maintained in order to achieve a high ammonia conversion. Similarly, the ammonia is completely decomposed over Ni-$BaCe_{0.4}Zr_{0.4}Y_{0.2}O_{3-\delta}$ (Ni/BCZY) above 600 °C.[92] The high ammonia conversion in case of Ni/BCZY is mainly due to high tolerance to hydrogen poisoning by accelerating the hydrogen spillover from nickel to catalyst support.

The anode supported single cell (Ni/BCZY//BCY10//BCY20-LSCF) was investigated in 550–700 °C temperature range with hydrogen and ammonia containing fuels. A maximum power density of 375 $mW \cdot cm^{-2}$ at 700 °C was achieved with hydrogen containing fuel. The performance of the cell was slightly lower in case of ammonia containing fuels (~350 $mW \cdot cm^{-2}$ at 700 °C) (Figure 14a). The cell showed slightly higher ohmic resistance for ammonia containing fuel compared to hydrogen throughout the temperature range, which can be attributed to the lower cell temperature due to the endothermic ammonia decomposition over the anode and thus the lower proton conductivity through the electrolyte (Figure 14b). The polarization resistance showed a large increase with reducing the operating temperature under both fuels, however, the R_p showed higher values using ammonia containing fuel throughout the temperature range compared to hydrogen containing fuel. The Bode plots of the impedance spectra (Figure 14c), indicated mainly two contributions, which are in the frequency

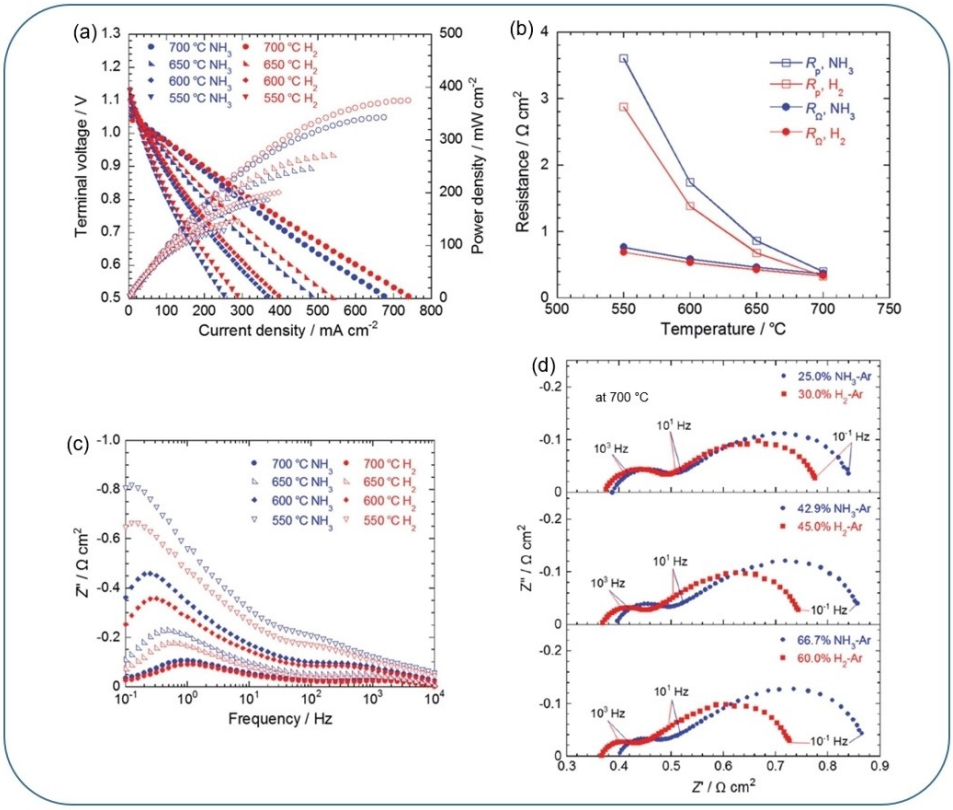

Figure 14. (a) I–V–P curves, (b) Ohmic and polarization resistances, (c) Bode plots of the impedance spectra of the anode supported Ni/BCZY//BCY20//BCY20-LSCF single cell in 550–700 °C temperature range using hydrogen and ammonia containing fuels, and (d) Nyquist plots at 700 °C with fuel gas at various concentrations. Reproduced from Ref. [92] with permission from the Royal Society of Chemistry.

range of 10^{-1}–10^{2} Hz and of 10^{2}–10^{3} Hz, similar to the work by Aoki et al.[160]

The contribution at 10^{2}–10^{3} Hz was attributed to the charge transfer process in the anode and its dependency on the fuel composition was not significant. The polarization resistance was dominated by the low frequency contribution and was attributed to the mass transfer process. The resistance for this contribution was significantly higher for ammonia containing fuels and was more prominent at lower temperature. This difference of hydrogen and ammonia containing fuels was ascribed to the different hydrogen diffusion process in the anode. By varying the ammonia concentration, the total resistance increased with increasing ammonia concentration. Contrarily, the total resistance decreased with increasing hydrogen content (Figure 14d). In the higher frequency range, the dependency of R_p was similar for both fuels, but the resistance in the low frequency process related to mass transfer process was reduced with increasing hydrogen in hydrogen fuels. In contrast, the resistance in the low frequency range increased for the cell with the higher supply of ammonia in the fuels.

Recently Nowicki et al.[91] reported the performance and electrochemical behavior of proton conducing tubular cell (active area 36 cm^2) using $BaCe_{0.7}Zr_{0.1}Y_{0.16}Zn_{0.04}O_{3-\delta}$ (BCZYZ) electrolyte, composite Ni/$BaCe_{0.7}Zr_{0.1}Y_{0.16}Zn_{0.04}O_{3-\delta}$ (Ni/BCZYZ) anode and $La_{0.8}Sr_{0.2}Co_{0.5}Fe_{0.5}O_{3-\delta}$/$BaCe_{0.7}Zr_{0.1}Y_{0.16}Zn_{0.04}O_{3-\delta}$ LSCF/BCZYZ cathode under pure ammonia as fuel. The cell showed a maximum power density of 0.236 $W\cdot cm^{-2}$ (8.5 W) at 750 °C. Moreover, the DRT analysis of impedance spectra revealed five peaks, among which the peaks P2, P3 and P5 were assigned for fuel electrode whereas peaks P1 and P4 to the oxygen electrode (Figure 15a). The process P5 was assigned to the gas diffusion process, P2 and P3 were assigned to H_2 protonation process *i.e.* diffusion of H_2 gas to the vicinity of the Ni surface and its adsorption/dissociation. With increasing ammonia flow rate at OCV and 750 °C, higher ohmic as well as polarization resistances were observed and the contribution in the middle frequency range was mainly affected as seen in the DRT plot (Figure 15a). Upon increasing the applied potential, an increase in R_p is observed (Figure 15b). When the operating temperature is reduced from 750 to 650 °C, the middle frequency peak shows the largest increase and is temperature dependent (Figure 15c). Some dissociative-adsorption processes coupled with the gas diffusion were suggested to explain such behavior. The performance of H^+-SOFC can be further improved by adding a catalytic layer of iron.[161] For example, Ni–Fe/BZCYYb//BZCYYb//PBSCF ($PrBa_{0.5}Sr_{0.5}Co_{1.5}Fe_{0.5}O_{5+\delta}$) single cell delivered a maximum power density of 1507 and 1078 $mW\cdot cm^{-2}$ at 700 °C with hydrogen an ammonia as fuel, respectively, which were lower for an electrode without iron coating, i.e. 1429 and 994 $mW\cdot cm^{-2}$ at 700 °C with hydrogen an ammonia as fuel,

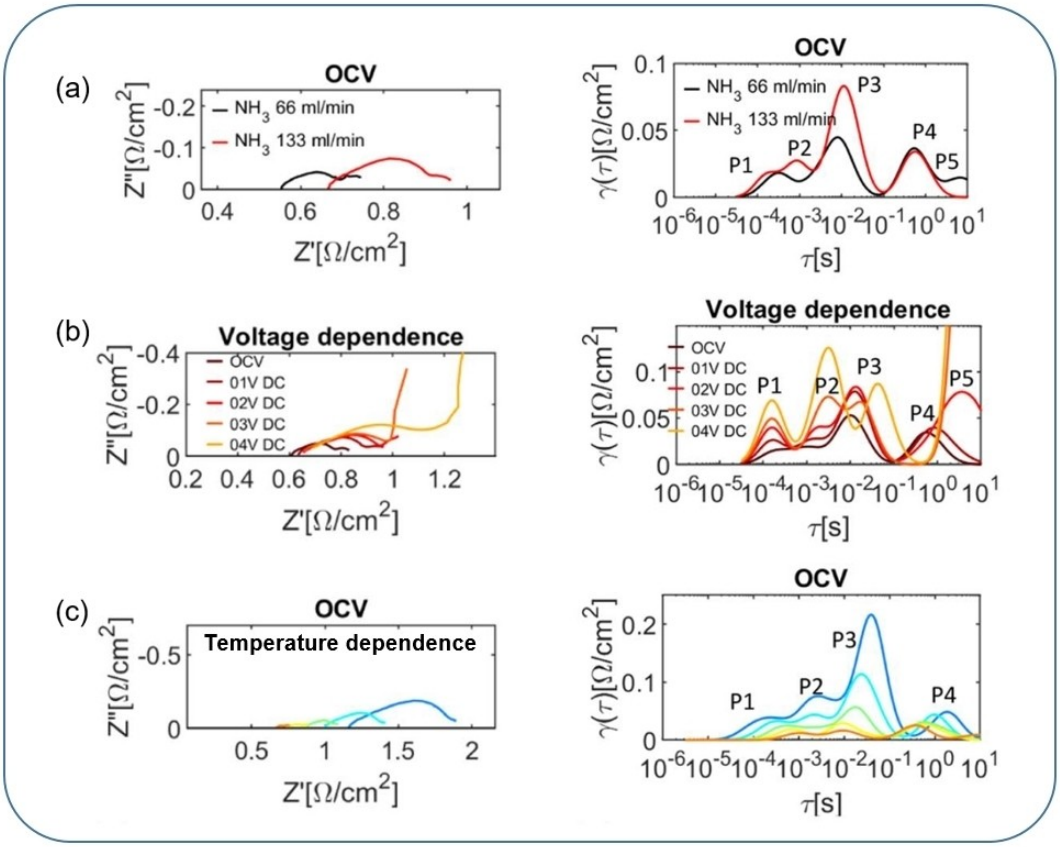

Figure 15. (a) Impedance spectra at OCV and corresponding DRT plots spectra of tubular cell at various flow rates of NH_3, (b) Impedance spectra at various applied DC voltage at 66 $ml\cdot min^{-1}$ flow of NH_3, and (c) Impedance spectra and DRT with temperature variation in 650–750 °C range under OCV conditions. Reproduced from Ref. [91] with permission from the Royal Society of Chemistry.

respectively. In the same context, Zhang et al.[162] reported results on the Fe-decorated Ni-BZCYYb//BZCYYb//PBSCF single cell under direct ammonia H^+-SOFC conditions and found a maximum power density of 1609 $mW \cdot cm^{-2}$ at 700 °C, while the performance without Fe decoration was significantly lower i.e. ~1400 $mW \cdot cm^{-2}$ at 700 °C. Therefore, it can be concluded that the addition of iron significantly improves the performance of single cells. The performance of different H^+-SOFC single cells with direct ammonia and hydrogen as fuel is summarized in Table 3.

As a summary about the H^+-SOFC, the proton conducting anode materials have a higher ammonia decomposition activity than oxide ion conductors due to their higher basicity. As a result, a slightly lower temperature is feasible for the complete ammonia decomposition. However, the observed performance of the single cells is slightly lower under ammonia fuel than under hydrogen especially at lower temperature $\leq$ 600 °C, mainly due to incomplete decomposition of ammonia. In addition, the ohmic and the polarization resistances of single cells in the presence of direct ammonia or fuels containing ammonia are somewhat higher than with fuels containing hydrogen. Long-term measurements of more than 1000 h with the single cells under direct ammonia fuel have not yet been carried out for the H^+-SOFC, to the best of our knowledge.

3.3. Direct Ammonia SOFC Stacks and Systems

For industrial applications, the scaling up of direct ammonia fuel cells is essential. In this aspect, Cinti et al.,[176] investigated the performance of a short stack supplied by Forschungszentrum Jülich, with four planar anode supported single cells fueled by pure and diluted ammonia (Figure 16a). The stack performance was compared at 700-800 °C under three different fuel gas compositions: a) pure hydrogen, b) simulated cracked ammonia (H_2/N_2), and c) pure NH_3, considering the same hydrogen amount at the end. The stack showed almost similar OCV and performance under the three tested gas compositions,

Table 3. Performance of single cells under direct ammonia and hydrogen as fuel for H^+-SOFC.

Single cell	Electrolyte thickness (μm)	T (°C)	Peak power density ($mW.cm^{-2}$)		Ref
			Ammonia fuel	H_2 fuel	
Ni-BZCY//BZCY//BSCF	35	700	390	420	171
		450	65	135	
Ni-BCZYYb//BZCYYbNi//BCFZY (BCZYYbNi: $BaCe_{0.7}Zr_{0.1}Y_{0.1}Yb_{0.1}Ni_{0.04}O_{3-\delta}$) (BCFZY: $BaCo_{0.4}Fe_{0.4}Zr_{0.1}Y_{0.1}O_{3-\delta}$)	4	650	877	944	172
		550	~650	~700	
		450	137	145	
Ni-BZCYYbPd//BZCYYb//BZFZY (BZCYYbPd: $Ba(Zr_{0.1}Ce_{0.7}Y_{0.1}Yb_{0.1})_{0.95}Pd_{0.05}O_{3-\delta}$) (BCZYYb: $BaCe_{0.7}Zr_{0.1}Y_{0.1}Yb_{0.1}O_{3-\delta}$)	20	650	600	860	173
		600	440	630	
		550	336	400	
Ni-BZCYYb//BZCYYb//BZFZY (BCZYYb: $BaCe_{0.7}Zr_{0.1}Y_{0.1}Yb_{0.1}O_{3-\delta}$)	20	650	450	694	173
		600	300	495	
		550	220	315	
Ni-CGO/BCGO/BSCF−CGO	~20	650	200	–	174
		600	147	–	
Pd//BZCY//BSCF	1	600	580	–	175
Ni-BZY//BZY//Pt	60-90	700	130	145	157
Ni–BCZY//BCY20//BCY20–LSCF	50-60	700	~345	~375	92
		650	~240	~270	
		600	~180	~200	
Ni-BCY25//BCY10//SSC	60	650	216	~240	159
		600	165	~180	
Ni-Fe/BZCYYb//BZCYYb//PBSCF	10	700	1609	~2100	162
		650	1257	–	
		600	723	–	
		550	360	–	
Ni-Fe/BZCYYb//BZCYYb//PBSCF (PBSCF: $PrBa_{0.5}Sr_{0.5}Co_{1.5}Fe_{0.5}O_{5+\delta}$)	10	700	1078	1507	161
		650	685	1157	
		600	327	776	
Ni/BCZYZ//BCZYZ//LSCF-BCZYZ (BCZYZ: $BaCe_{0.7}Zr_{0.1}Y_{0.16}Zn_{0.04}O_{3-\delta}$)	50	750	236	–	91

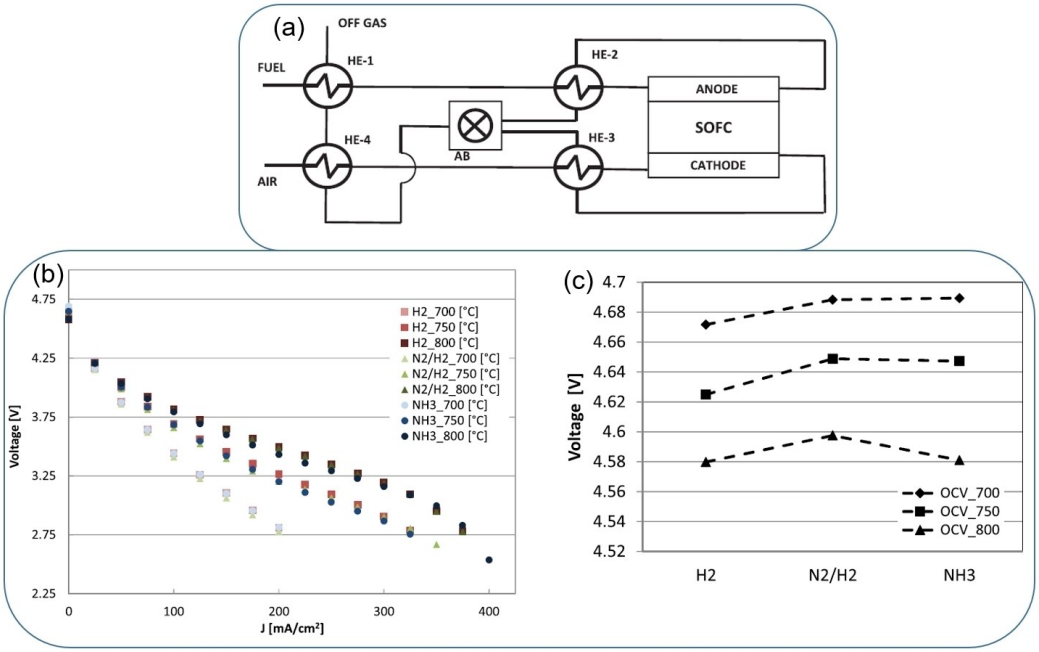

Figure 16. (a) Schematic diagram of the SOFC System, (b) I–V curves, and (c) variation of OCV with different fuel gas compositions. Reproduced with permission.[176] Copyright 2016, Elsevier.

although, the temperature of the stack was decreased by 3 °C in case of direct fueled ammonia because of endothermal cracking reaction (Figure 16 b, c). It was also demonstrated that the stack operation under direct ammonia as a fuel requires a smaller flow rate than the one used with hydrogen, which increases the efficiency up to 22% when the system is fueled with ammonia compared with a gaseous mixture with the same amount of hydrogen and nitrogen. Moreover, the operation of SOFC with diluted ammonia showed an efficiency of 50%. This is remarkable as the diluted ammonia is not toxic, not flammable and can be easily handled. In another work, Okanishi et al.[177] investigated a 200 W SOFC stack comprised of 10 planar anode supported single cells (NiO/YSZ anode) with 95 cm^2 active area. The stack performance was slightly lower in direct ammonia fuel compared to the H_2 fuel, especially above 5 A. The stacked delivered a power of 250, 232 and 234 W at 36 V at 770 °C under direct ammonia, decomposed ammonia and autothermally cracked ammonia fueled systems, respectively.

In an autothermal ammonia cracker, a small amount of air or oxygen is added to the supplied ammonia to oxidize it and to produce the heat required for decomposing the remaining ammonia. Hence, the heat recovery from the exhaust gas is not required. The electrical efficiencies at 36 A were found to be 36.3, 39.1 and 29.1% for the direct ammonia fueled, decomposed ammonia fueled and autothermally cracked ammonia fueled systems, respectively. The fuel utilization was also relatively lower (62% at 36 A), ideally it should be more than 70–80% for practical application. Barelli et al.[178] investigated a SOFC short-stack (supplied by SOLIDpower, Mezzolombardo, Italy) consisted of 6 planar anode supported cells (NiO/YSZ anode and LSCF + GDC cathode) with a total active area of 80 cm^2 and reported a net power density of 0.36 $W \cdot cm^{-2}$ at 0.78 V and 750 °C. The stack showed an electrical efficiency of 52.1% with direct ammonia as fuel, however, a higher electrical efficiency of 60% was achieved when externally cracked ammonia was used. The performance of the same stack was also reported by Zendrini et al.[179] and a power density of 0.35 $W \cdot cm^{-2}$ (28 A) at 0.79 V and 760 °C was obtained with ammonia fuel with 48% of electrical efficiency.

Kishimoto et al.[180] investigated a SOFC stack with 30 anode supported single cells (diameter 120 mm and active area 95 cm^2) and obtained 1 kW power output with 52% direct current (DC) electrical efficiency. They investigated the performance of the stack under three different conditions: a) direct ammonia decomposition in the SOFC stack system, b) combining the SOFC system with external ammonia cracker using BaO/Ni/Sm_2O_3/MgO catalysts, and c) combining the SOFC system with autothermal ammonia cracker using Co–Ce-Zr composite oxide catalysts. A maximum power density of 0.368 $W \cdot cm^{-2}$ (1048 W) was achieved at a current load of 0.526 $A \cdot cm^{-2}$ (50 A) (Figure 17 a). The performance of the stack fueled with direct ammonia was slightly lower than that of the stack fueled with hydrogen-nitrogen mixture (H_2:N_2, 3:1), mainly due to a temperature drop within the stack due to an endothermic ammonia decomposition reaction. The temperature of the bottom separator was found to decrease by 15 °C. The performance of the SOFC stack fueled with externally decomposed ammonia (external ammonia cracker or autothermal ammonia cracker) and that of the stack fueled with a hydrogen-nitrogen mixture (H_2:N_2, 3:1) is almost the same (Figure 17 b, c), as no temperature drop was observed due to endothermic ammonia decomposition reaction. However, the stack voltage at OCV conditions was slightly lower compared to direct ammonia fuel

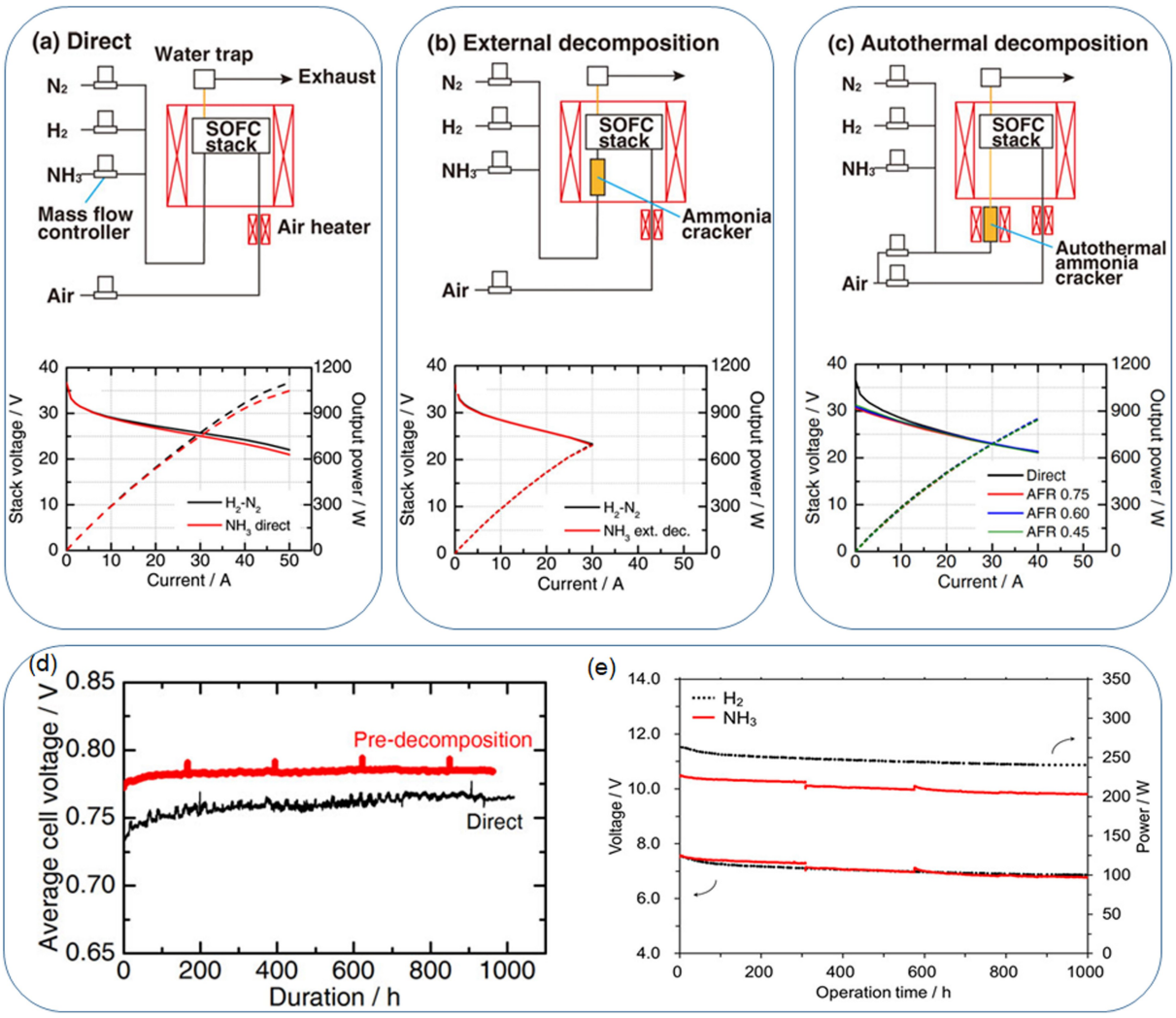

Figure 17. Schematic flow diagram and I–V–P curve for (a) the direct ammonia fueled SOFC system, (b) the combined system of an external ammonia cracker and SOFC stack, (c) the combined system of an autothermal ammonia cracker and an SOFC stack (AFR stands for air-to-fuel ratio), (d) variation of stack voltage at a current load of 30 A (0.316 A·cm^{-2}) for the direct ammonia and externally cracked ammonia fueled SOFC stack during durability test up to 1000 h at 750 °C, Reproduced from Ref. [180] Copyright (2020), with permission from Wiley-VCH, (e) variation of the stack voltage at a current load of 30 and 35 A for the direct ammonia and H_2 fueled SOFC stack respectively at 770 °C. Reproduced from Ref. [177] Copyright (2017), with permission from Wiley-VCH.

due to the contained steam in the fuel from the autothermal reactor.

The stack fueled with direct ammonia as well as externally decomposed ammonia showed excellent stability during long-term operation up to 1000 h. When the stack is operated with direct ammonia as a fuel, a slight decrease in the average cell voltage was observed at the beginning of the long-term test, however, it was recovered during the first 200 h of operation and then the voltage was stable up to 1000 h, similar to the stack fueled with decomposed ammonia (Figure 17 d). Moreover, after completing the long-term test, stack components were analyzed by scanning electron microscopy and electron probe analysis (EPMA). No change in the anode and cathode of the single cells in comparison to initial microstructure of the cell was found, however, the surface of the separators was affected by the direct ammonia fuel. It was significantly deformed, and Fe rich particles were observed at the surface. In addition, the nitrogen is also detected in the bulk of the separator, which indicates the nitride formation with the separator material (SUS430).

In another work, the direct ammonia fueled 200 W SOFC stack showed a slight drop in the stack voltage during the stability test up to 1000 h at 770 °C. However, its stability was almost comparable to that of the hydrogen fueled stack,[177] as depicted in Figure 17e. The direct ammonia fueled SOFC maintained the power output above 200 W without significant degradation. Moreover, the exhaust gas from the stack did not detect any NO_x species such as NO, N_2O and NO_2 during the stability test. These long-term measurements results confirm that the SOFC fueled with ammonia is a promising power generation device with high long-term stability.

As a summary for direct ammonia-SOFC stacks and systems, the measurements were only carried out for O^{2-}-SOFC. So far, the state-of-the-art Ni-YSZ anode has been used in the stack

and has shown promising behavior and complete dissociation of ammonia at elevated temperatures above 700 °C. Furthermore, no NO_x formation has been observed. The performance behavior of the SOFC stack fueled under direct ammonia shows a slightly lower performance with ammonia than with simulated ammonia as fuels, which is mainly due to the endothermic ammonia decomposition. Most importantly, the long-term degradation behavior with direct ammonia and simulated ammonia as fuel showed a similar and stable behavior up to 1000 hours under current load. In the *post test* analysis, no change was evidenced in the anode and cathode of the cells in comparison to the initial microstructure of the cell. However, nitride formation was detected in the SUS430 interconnect.

Despite direct ammonia fuel cells offering several advantages, there are some challenges in scaling up direct ammonia fuel cells, such as the relatively lower electrochemical performance of ammonia-fueled SOFCs compared to hydrogen fuel cells, especially at lower operating temperatures below 700 °C, mainly due to the dilution of the hydrogen with nitrogen (as well as steam in the case of O^{2-}-SOFCs). However, this can be mitigated by introducing active catalysts and further decreasing the thickness of the electrolyte layer.[181] Moreover, the stability of the SOFC stack components such as electrodes, contact materials, sealing materials, connections and piping materials under ammonia or even ammonia and steam for O^{2-}-SOFCs have not been fully examined, as ammonia reacts with water and forms a very corrosive liquid or NO_x during combustion. Therefore, this should be investigated and further optimization should be carried out comprehensively. In addition, nitride formation in electrode and interconnect materials is another problem during long term with direct ammonia fuel cells, particularly at low temperatures below 700 °C.

4. Challenges

Although ammonia is a potential energy carrier, there are safety and technological challenges that need to be addressed before ammonia can be successfully integrated as a primary energy vector in the hydrogen economy. Some of the key problematics in this regard are listed below and the potential solutions are proposed thereinafter.

a) Risk of ammonia and hydrogen leaks:

There is a potential risk of leakage of NH_3 during its storage, transportation, conversion into H_2 and its use in the fuel cell devices, which can be serious and life threatening. NH_3 is known to be toxic to humans even at very low concentration exposure, such that occupational safety of health administration (OSHA) recommends a short-term exposure limit of NH_3 ca. 25 ppm. Although, it has a pronounced pungent odor and can be detected by the human nose at concentrations as low as 20 ppm in the air, preventive measures needs to be taken for continuous monitoring of possible leakage scenario.[182] There is also a significant risk associated to H_2 leak from the indirect NH_3-H_2 fuel cell devices, where H_2 is produced *in situ* from NH_3 decomposition, owing to its high permeability, detonation power and inflammability. Moreover, H_2 is an odorless and colorless gas, making it difficult to detect. Therefore, a comprehensive monitoring system needs to be put in place to safeguard workers and users' safety. Regarding NH_3 leak monitoring, different microsensor systems have been developed, based on metal oxides and organic semiconducting materials,[183–186] demonstrating detection of NH_3 concentration in the sub-ppm range and displaying high operation stability and reproducibility. In particular, the organic semiconductor based NH_3 sensors are highly appealing owing to their room temperature operation and detection limit down to a few hundred ppb.[187–191] These sensors utilize low-cost organic molecular materials, such as metal phthalocyanines and porphyrins as an active layer, are flexible and can be integrated in the complex measuring environment, such as in fuel cells. On site H_2 leak detection is a major research topic currently to develop low-cost, sensitive and robust H_2 sensors. Different types of sensor systems based on multitudes of sensing nanomaterials are being investigated,[192–194] reporting detection of H_2 down to a few ppb, high selectivity and robust performance in harsh working conditions. The performance of such sensor systems should be further validated in fuel cell devices to detect potential H_2 leak.

b) Electrode microstructure modification and nitride formation:

Despite the numerous advantages of direct ammonia SOFC systems, there are some issues that need to be addressed. In direct ammonia SOFCs, the ammonia is fed directly to the anode. If the ammonia does not decompose completely, it can react according to equation 16 with the Ni-containing cermet and form nickel nitride (Ni_3N, eq. 16). The nickel-containing anode should also be able to avoid redox reactions to split ammonia, or else Ni_3N will form from the Ni particles in the anode. This leads to volumetric changes in the anode microstructure and thus to an increase in the overvoltage of the cell and thus to a delamination of the electrode and severe degradation during long-term use.

$$3Ni + NH_3 \rightarrow Ni_3N + 1.5H_2 \quad (16)$$

The performance of the SOFC stack degrades with ammonia as fuel as the nickel catalyst causes nitride formation.[165,180,195] The enlargement of the Ni particles, formation of microscopic pores and agglomerations in the metallic nickel particles were also observed due to their nitride formation. Similar behavior was observed for single cells, and it was observed that the formation of Ni_3N leads to morphological and structural changes in the Ni-YSZ anode, thus affecting the long-term stability of direct ammonia SOFC.[196] Moreover, the nitride formation was also observed in the SUS430 interconnect of the SOFC stack.[180]

c) Emission of NO_x

This is mainly observed with the O^{2-}-SOFC, when the oxide ion transported from cathode to anode and reacts with ammonia or nitrogen in the anode chamber and not with hydrogen. In this case the formation of NO (eq. 14) is observed.[197] However, this is not an issue with the H^+-SOFC. Moreover, the H_2O is generated in O^{2-}-SOFC at the anode and

mixed with the exhaust gas containing small amount of undissociated ammonia leads to the formation of a very corrosive liquid or NO_x when combusted. This can further damage the SOFC interconnects, gas lines and metallic tubes of the whole SOFC system. Also, the emission of toxic NO_x can impact the air quality, leading to human and environmental concerns.

5. Summary and Outlooks

To sum up, ammonia will play an important role in the future energy supply due to its favorable physical properties and the existing infrastructure for transport, storage and distribution. The present review article assesses the role of NH_3 in the green hydrogen economy and reports the technological advancements made in NH_3 decomposition to produce hydrogen and finally its use in the fuel cell devices. For the NH_3-to-H_2 production, significant advancements have been made in four methodologies, involving thermocatalytic, oxidative, electrocatalytic and photocatalytic decomposition. Among these methods, one of the widely investigated method has been the thermocatalytic cracking of ammonia. The research focus in this approach of H_2 production was to decrease the NH_3 cracking temperature, improving the NH_3 conversion efficiencies and fastening the rate of H_2 production. To achieve these objectives, the key strategy has been to use Ru and Ru-based alloy catalysts, which demonstrated very high catalytic activity and could successfully decrease the NH_3 decomposition temperature to *ca.* 400 °C with high H_2 production rate. In the last couple of years, significant advancements were made to develop non-noble metal based low-cost metal catalysts as an alternative to expensive and scarce Ru-based materials. In the endeavor, notable progress has been made in the development of Ni, Co, Fe and alloys catalysts, which can attain the similar H_2 production rate as of Ru-based catalysts, but at higher reaction temperature. To overcome the requirement of high temperature in the NH_3 decomposition, the idea of oxidative decomposition of NH_3 was perceived, exploiting the exothermic nature of NH_3 oxidation reaction, in which a fraction of input NH_3 feed is oxidized *in situ* on the catalytic bed, rising the temperature enough to induce thermocatalytic cleavage of NH_3. However, the use of Ru-based catalysts and requirement for high temperature pre-treatment of the catalytic bed limit the widescale use of such materials. For the room temperature decomposition of NH_3, electrocatalytic and photocatalytic decomposition approaches have proved highly effective and have attracted many interests in the last decade. In particular, the electrolysis of NH_3 to produce H_2 has witnessed significant advancement, which has been performed in aqueous, organic and pure NH_3 solution. The research focus in this area has been the ammonia electrooxidation reaction and development of efficient and durable electrocatalysts. Different Pt and associated alloys-based materials were studied, demonstrating high activity in splitting NH_3. However, the harsh electrolysis conditions, especially in the alkaline aqueous medium proved highly detrimental for the stability of Pt-based electrocatalysts. Other non-noble metal-based materials dispersed over large surface area porous metal or metal oxide supports have been also investigated, which are cheaper and abundantly available. In this direction, the developments made with Cu_2O, Fe_3N_2 and $Ni(OH)_2$ based electrocatalysts are worth mentioning, which demonstrate similar or superior H_2 production rates as of Pt-based material and can endure the harsh electrolysis conditions. Moreover, notable results have been reported on the use of coordination complexes of metals in the homogeneous and heterogeneous electrocatalytic decomposition of NH_3. In particular, the recent developments on Fe based complexes are highly encouraging, demonstrating ca. 150 equivalent of N_2 production per equivalent of the electrocatalyst in aqueous NH_3 solution.

Regarding the advancements made in the NH_3 or H_2 utilization technologies to produce energy, SOFCs based devices have attracted considerable attention. In this review, we have addressed the performance, electrochemistry and long-term stability of high temperature SOFCs fueled with direct ammonia and compared them with pure hydrogen and simulated ammonia (H_2:N_2 = 3:1). In addition, the technological challenges of ammonia cracking in the context of direct ammonia SOFCs, emerging anode materials for direct ammonia SOFCs and future prospects for the transition to the power generation from ammonia are discussed. As far as the component materials are concerned, both the direct ammonia O^{2-}-SOFCs and the H^+-SOFCs are still based on the materials used for the hydrogen SOFCs. These are 8YSZ electrolytes, Ni-YSZ cermet anodes and La-based perovskite cathodes for the O^{2-}-SOFCs and BCZY-based electrolytes, Ni-BCZY cermet anodes and perovskite cathodes for the H^+-SOFCs. In recent times, the majority of research activities have focused on the development of anode catalysts to improve ammonia decomposition and performance of direct ammonia SOFCs. Especially for the anode materials for O^{2-}-SOFC, cermet-based anodes, *i.e.* Ni-YSZ or Ni-doped cerium oxide, showed promising behavior and exhibited complete dissociation of ammonia at temperature above 700 °C, and furthermore no NO_x formation has been detected so far. The performance behavior of the single cells showed a higher performance with hydrogen than with ammonia as fuel, which is mainly due to the dilution effect of the fuel with nitrogen and the hydrogen poisoning effect. The ohmic and the polarization resistances are slightly higher under ammonia fuel than under pure hydrogen owing to the endothermic ammonia decomposition reaction that lowers the cell temperatures, in addition to the dilution of the fuel gas. It is worth noting that with very active catalysts, the performance is the same for ammonia and hydrogen as fuel. Moreover, with direct ammonia and simulated ammonia as fuel, interestingly, the single cells or stacks show similar performance behavior, especially at higher operating temperatures above ~800 °C. Despite several advantages of direct ammonia SOFCs, one of the main problems in the development of direct ammonia O^{2-}-SOFC is the coarsening of nickel particles and the formation of nickel nitride in the cermet-based anodes during long-term operation. Research is therefore ongoing into the development of new electrode materials (perovskites, catalysts infiltrated in perovskites and ceramic oxides; YSZ, GDC *etc.*), which have a higher ammonia

decomposition activity, stability, improve the problems of catalyst poisoning and microstructural degradation and have a lower NO_x formation ability particularly at lower temperatures. In the case of H^+-SOFC, there has not been much done yet. In general, proton conducting anode materials have a higher ammonia decomposition activity than oxide ion conductors due to their higher basicity. As a result, a slightly lower temperature of ~600 °C is feasible for the complete ammonia decomposition. However, the performance of the single cells is again slightly lower under ammonia fuel than hydrogen especially at lower temperature $\leq$600 °C. Long-term measurements with large single cells and stacks still need to be carried out to confirm the advantages of H^+-SOFCs.

To enable the commercialization of direct ammonia SOFC for power generation, further research is needed to improve the technological challenges. In this respect, the development of new materials for cell components, particularly the anodes and interconnectors, is extremely important for the direct and efficient conversion of ammonia into electrical energy, as these are in direct contact with ammonia during operation. Ruthenium (Ru) is a highly active catalyst and could in future play a decisive role in ammonia decomposition/splitting at lower temperatures compared to a conventional Ni-based catalyst, resulting in significantly lower energy consumption. However, due to the high costs, the development of Ru-based catalysts on a large scale is very difficult. Nevertheless, it is possible to develop a new Ru-based catalyst by combining non-precious metals to achieve a high catalytic synergy effect.

With the current state-of-the-art Ni-YSZ anode and the interconnect materials, the formation of nitrides is one of the challenges. To mitigate this, new anode catalysts and interconnect materials must be developed. In addition, the coating on interconnect materials need to be investigated to avoid corrosion. Since cermet anodes containing NiFe alloys perform significantly better than Ni cermets, the performance and long-term behavior of other Fe-containing anodes, especially single-phase perovskite-based catalysts should be investigated under direct ammonia fuel cell conditions. Lastly, the H^+-SOFC has some advantages over O^{2-}-SOFC, as water vapor is generated on the cathode side, which can reduce the risk of corrosion of cell or stack components as well as NO_x emissions. However, long-term measurements must be carried out with large single cells as well as with stacks using ammonia directly as fuel.

Acknowledgements

The authors (A.K. & M.B.) thank Université de Bourgogne to provide financial support through PO FEDER-FSE Bourgogne 2019/2022 (via CoMICS program) and Agence Nationale de la Recherche (ANR) through the project OUTSMART ANR-2015-CE39-0004-03. The authors (V.V., L.N., B.D.H., & R.A.E.) also thank the Helmholtz Association for the financial support of the SOC research and development at Forschungszentrum Jülich. Open Access funding enabled and organized by Projekt DEAL.

Conflict of Interests

The authors declare no conflict of interest.

Data Availability Statement

The data that support the findings of this study are available from the corresponding author upon reasonable request.

Keywords: Ammonia cracking · Hydrogen production · Electrocatalysts · Fuel cells · SOFC

[1] H. D. Matthews, S. Wynes, *Science.* **2022**, *376*, 1404–1409.
[2] K. T. Møller, T. R. Jensen, E. Akiba, H.-w. Li, *Prog. Nat. Sci.: Mater.* **2017**, *27*, 34–40.
[3] T. He, P. Pachfule, H. Wu, Q. Xu, P. Chen, *Nat. Rev. Mater.* **2016**, *1*, 16059.
[4] G. Santos, *Transp. Policy.* **2017**, *59*, 71–74.
[5] O. Bethoux, *Energies* **2020**, *13(21)*, 5843.
[6] N. Konno, S. Mizuno, H. Nakaji, Y. Ishikawa, *SAE Int. J. Alt. Power.* **2015**, *4*, 123–129.
[7] P. J. Megía, A. J. Vizcaíno, J. A. Calles, A. Carrero, *Energy Fuels.* **2021**, *35*, 16403–16415.
[8] T. Yusaf, M. Laimon, W. Alrefae, K. Kadirgama, H. A. Dhahad, D. Ramasamy, M. K. Kamarulzaman, B. Yousif, *Appl. Sci.* **2022**, *12*, 781.
[9] M. Wappler, D. Unguder, X. Lu, H. Ohlmeyer, H. Teschke, W. Lueke, *Int. J. Hydrogen Energy.* **2022**, *47*, 33551–33570.
[10] M. Asif, S. Sidra Bibi, S. Ahmed, M. Irshad, M. Shakir Hussain, H. Zeb, M. Kashif Khan, J. Kim, *Chem. Eng. J.* **2023**, *473*, 145381.
[11] X. Wang, W. Gao, *Int. J. Hydrogen Energy.* **2023**, *48*, 35795–35808.
[12] P. C. Okonkwo, E. M. Barhoumi, I. Ben Belgacem, I. B. Mansir, M. Aliyu, W. Emori, P. C. Uzoma, W. H. Beitelmal, E. Akyüz, A. B. Radwan, R. A. Shakoor, *Int. J. Hydrogen Energy* **2023**, *48*, 12935–12948.
[13] Y. Zhao, B. P. Setzler, J. Wang, J. Nash, T. Wang, B. Xu, Y. Yan, *Joule.* **2019**, *3*, 2472–2484.
[14] N. Itoh, Y. Kikuchi, T. Furusawa, T. Sato, *Int. J. Hydrogen Energy* **2021**, *46*, 20257–20265.
[15] Z. Wan, Y. Tao, J. Shao, Y. Zhang, H. You, *Energy Convers. Manage.* **2021**, *228*, 113729.
[16] B. S. Zainal, P. J. Ker, H. Mohamed, H. C. Ong, I. M. R. Fattah, S. M. A. Rahman, L. D. Nghiem, T. M. I. Mahlia, *Renewable Sustainable Energy Rev.*. **2024**, *189*, 113941.
[17] I. Lucentini, X. Garcia, X. Vendrell, J. Llorca, *Ind. Eng. Chem. Res.* **2021**, *60*, 18560–18611.
[18] S. Mukherjee, S. V. Devaguptapu, A. Sviripa, C. R. F. Lund, G. Wu, *Appl. Catal. B* **2018**, *226*, 162–181.
[19] J. Lee, S. Ga, D. Lim, S. Lee, H. Cho, J. Kim, *Chem. Eng. J.* **2023**, *457*, 141203.
[20] R. Sitar, J. Shah, Z. Zhang, H. Wikoff, J. D. Way, C. A. Wolden, *J. Membr. Sci.* **2022**, *644*, 120147.
[21] K. Siddharth, Y. Chan, L. Wang, M. Shao, *Curr. Opin. Electrochem.* **2018**, *9*, 151–157.
[22] N. Hanada, S. Hino, T. Ichikawa, H. Suzuki, K. Takai, Y. Kojima, *Chem. Commun.* **2010**, *46*, 7775–7777.
[23] T. Matsunaga, S. Matsumoto, R. Tasaki, Y. Ogura, T. Eboshi, Y. Takeishi, K. Honda, K. Sato, K. Nagaoka, *ACS Sustainable Chem. Eng.* **2020**, *8*, 13369–13376.
[24] D. J. Little, I. I. I. M. R. Smith, T. W. Hamann, *Energy Environ. Sci.* **2015**, *8*, 2775–2781.
[25] E. Spatolisano, L. A. Pellegrini, A. R. de Angelis, S. Cattaneo, E. Roccaro, *Ind. Eng. Chem. Res.* **2023**, *62*, 10813–10827.
[26] T. V. Choudhary, A. K. Santra, C. Sivadinarayana, B. K. Min, C. W. Yi, K. Davis, D. W. Goodman, *Catal. Lett.* **2001**, *77*, 1–5.
[27] V. Alagharu, S. Palanki, K. N. West, *J. Power Sources.* **2010**, *195*, 829–833.
[28] F. Chang, W. Gao, J. Guo, P. Chen, *Adv. Mater.* **2021**, *33*, 2005721.
[29] C. Chen, K. Wu, H. Ren, C. Zhou, Y. Luo, L. Lin, C. Au, L. Jiang, *Energy Fuels.* **2021**, *35*, 11693–11706.

[30] S. Mazzone, T. Goklany, G. Zhang, J. Tan, E. I. Papaioannou, F. R. García-García, *Appl. Catal. A* **2022**, *632*, 118484.
[31] Z. Su, J. Guan, Y. Liu, D. Shi, Q. Wu, K. Chen, Y. Zhang, H. Li, *Int. J. Hydrogen Energy.* **2024**, *51*, 1019–1043.
[32] T. Su, B. Guan, J. Zhou, C. Zheng, J. Guo, J. Chen, Y. Zhang, Y. Yuan, W. Xie, N. Zhou, H. Dang, B. Xu, Z. Huang, *Energy Fuels.* **2023**, *37*, 8099–8127.
[33] J. C. Ganley, F. S. Thomas, E. G. Seebauer, R. I. Masel, *Catal. Lett.* **2004**, *96*, 117–122.
[34] S.-F. Yin, Q.-H. Zhang, B.-Q. Xu, W.-X. Zhu, C.-F. Ng, C.-T. Au, *J. Catal.* **2004**, *224*, 384–396.
[35] J. Chen, Z. H. Zhu, S. Wang, Q. Ma, V. Rudolph, G. Q. Lu, *Chem. Eng. J.* **2010**, *156*, 404–410.
[36] S. J. Wang, S. F. Yin, L. Li, B. Q. Xu, C. F. Ng, C. T. Au, *Appl. Catal. B* **2004**, *52*, 287–299.
[37] A. M. Karim, V. Prasad, G. Mpourmpakis, W. W. Lonergan, A. I. Frenkel, J. G. Chen, D. G. Vlachos, *J. Am. Chem. Soc.* **2009**, *131*, 12230–12239.
[38] H. J. Lee, E. D. Park, *Catalysts* **2022**, *12*, 1203.
[39] S. Kang, J. Cha, Y. S. Jo, Y.-J. Lee, H. Sohn, Y. Kim, C. K. Song, Y. Kim, D.-H. Lim, J. Park, C. W. Yoon, *Adv. Mater.* **2023**, *35*, 2203364.
[40] H. Fang, S. Wu, T. Ayvali, J. Zheng, J. Fellowes, P.-L. Ho, K. C. Leung, A. Large, G. Held, R. Kato, K. Suenaga, Y. I. A. Reyes, H. V. Thang, H.-Y. T. Chen, S. C. E. Tsang *Nat. Commun.* **2023**, *14*, 647.
[41] T. E. Bell, L. Torrente-Murciano, *Top. Catal.* **2016**, *59*, 1438–1457.
[42] K. Okura, T. Okanishi, H. Muroyama, T. Matsui, K. Eguchi, *Appl. Catal. A* **2015**, *505*, 77–85.
[43] W. U. Khan, H. S. Alasiri, S. A. Ali, M. M. Hossain, *Chem. Rec.* **2022**, *22*, e202200030.
[44] J. Yang, D. He, W. Chen, W. Zhu, H. Zhang, S. Ren, X. Wang, Q. Yang, Y. Wu, Y. Li, *ACS Appl. Mater. Interfaces.* **2017**, *9*, 39450–39455.
[45] P. Xie, Y. Yao, Z. Huang, Z. Liu, J. Zhang, T. Li, G. Wang, R. Shahbazian-Yassar, L. Hu, C. Wang, *Nat. Commun.* **2019**, *10*, 4011.
[46] K. Nagaoka, T. Eboshi, Y. Takeishi, R. Tasaki, K. Honda, K. Imamura, K. Sato, *Sci. Adv.* **2017**, *3(4)*, e1602747.
[47] D. Chakraborty, C. D. Damsgaard, H. Silva, C. Conradsen, J. L. Olsen, H. W. P. Carvalho, B. Mutz, T. Bligaard, M. J. Hoffmann, J.-D. Grunwaldt, F. Studt, I. Chorkendorff, *Angew. Chem. Int. Ed.* **2017**, *56*, 8711–8715.
[48] K. Obata, K. Kishishita, A. Okemoto, K. Taniya, Y. Ichihashi, S. Nishiyama, *Appl. Catal. B* **2014**, *160–161*, 200–203.
[49] S. Zhang, Z. He, X. Li, J. Zhang, Q. Zang, S. Wang, *Nanoscale Adv.* **2020**, *2*, 3610–3623.
[50] M. Kaneko, N. Gokan, N. Katakura, Y. Takei, M. Hoshino, *Chem. Commun.* **2005**, 1625–1627.
[51] H. Yuzawa, T. Mori, H. Itoh, H. Yoshida, *J. Phys. Chem. C.* **2012**, *116*, 4126–4136.
[52] H. Kominami, H. Nishimune, Y. Ohta, Y. Arakawa, T. Inaba, *Appl. Catal. B* **2012**, *111–112*, 297–302.
[53] Y. Shiraishi, S. Toi, S. Ichikawa, T. Hirai, *ACS Appl. Nano Mater.* **2020**, *3*, 1612–1620.
[54] M. Reli, M. Edelmannová, M. Šihor, P. Praus, L. Svoboda, K. K. Mamulová, H. Otoupalíková, L. Čapek, A. Hospodková, L. Obalová, K. Kočí, *Int. J. Hydrogen Energy.* **2015**, *40*, 8530–8538.
[55] A. Iwase, K. Ii, A. Kudo, *Chem. Commun.* **2018**, *54*, 6117–6119.
[56] Z. Wu, N. Ambrožová, E. Eftekhari, N. Aravindakshan, W. Wang, Q. Wang, S. Zhang, K. Kočí, Q. Li, *Emergent Materials.* **2019**, *2*, 303–311.
[57] B. Zhou, N. Zhang, Y. Wu, W. Yang, Y. Lu, Y. Wang, S. Wang J Energy, *Chem.* **2021**, *60*, 384–402.
[58] J. H. Jang, S. Y. Park, D. H. Youn, Y. J. Jang, *Catalysts* **2023**, *13*, 803.
[59] C. Zhong, W. B. Hu, Y. F. Cheng, *J. Mater. Chem. A.* **2013**, *1*, 3216–3238.
[60] J. Łuczak, M. Lieder, *Adv. Colloid Interface Sci.* **2023**, *319*, 102963.
[61] H. Kim, S. Hong, H. Kim, Y. Jun, S. Y. Kim, S. H. Ahn, *Appl. Mater. Today.* **2022**, *29*, 101640.
[62] F. J. Vidal-Iglesias, N. García-Aráez, V. Montiel, J. M. Feliu, A. Aldaz, *Electrochem. Commun.* **2003**, *5*, 22–26.
[63] C. Zhang, S. Y. Hwang, Z. Peng J Mater, *Chem. A.* **2013**, *1*, 14402–14408.
[64] S. Johnston, B. H. R. Suryanto, D. R. MacFarlane, *Electrochim. Acta.* **2019**, *297*, 778–783.
[65] N. Hanada, Y. Kohase, K. Hori, H. Sugime, S. Noda, *Electrochim. Acta.* **2020**, *341*, 136027.
[66] W. Peng, L. Xiao, B. Huang, L. Zhuang, J. Lu, *J. Phys. Chem. C.* **2011**, *115*, 23050–23056.
[67] X. Yang, H. Sun, C. Liu, L. Yu, H. Chen, *Chem. Eng. J.* **2022**, *442*, 136167.
[68] H. Kim, W. Yang, W. H. Lee, M. H. Han, J. Moon, C. Jeon, D. Kim, S. G. Ji, K. H. Chae, K.-S. Lee, J. Seo, H.-S. Oh, H. Kim, C. H. Choi, *ACS Catal.* **2020**, *10*, 11674–11684.
[69] Y. T. Chan, K. Siddharth, M. Shao, *Nano Res.* **2020**, *13*, 1920–1927.
[70] J. Huang, Z. Chen, J. Cai, Y. Jin, T. Wang, J. Wang, *Nano Res.* **2022**, *15*, 5987–5994.
[71] W. Xu, R. Lan, D. Du, J. Humphreys, M. Walker, Z. Wu, H. Wang, S. Tao, *Appl. Catal. B* **2017**, *218*, 470–479.
[72] J. Huang, J. Cai, J. Wang, *ACS Appl. Energ. Mater.* **2020**, *3*, 4108–4113.
[73] D. J. Little, D. O. Edwards, M. R. Smith III, T. W. Hamann, *ACS Appl. Mater. Interfaces.* **2017**, *9*, 16228–16235.
[74] M. D. Zott, P. Garrido-Barros, J. C. Peters, *ACS Catal.* **2019**, *9*, 10101–10108.
[75] M. D. Zott, J. C. Peters, *J. Am. Chem. Soc.*. **2021**, *143*, 7612–7616.
[76] H.-Y. Liu, H. M. C. Lant, C. C. Cody, J. Jelušić, R. H. Crabtree, G. W. Brudvig, *ACS Catal.* **2023**, *13*, 4675–4682.
[77] C. Costentin, S. Drouet, M. Robert, J.-M. Savéant, *J. Am. Chem. Soc.* **2012**, *134*, 11235–11242.
[78] P. L. Dunn, S. I. Johnson, W. Kaminsky, R. M. Bullock, *J. Am. Chem. Soc.* **2020**, *142*, 3361–3365.
[79] P. Bhattacharya, Z. M. Heiden, G. M. Chambers, S. I. Johnson, R. M. Bullock, M. T. Mock, *Angew. Chem. Int. Ed.* **2019**, *58*, 11618–11624.
[80] K. Nakajima, H. Toda, K. Sakata, Y. Nishibayashi, *Nat. Chem.* **2019**, *11*, 702–709.
[81] F. Habibzadeh, S. L. Miller, T. W. Hamann, M. R. Smith, *Proc. Nat. Acad. Sci.* **2019**, *116*, 2849–2853.
[82] I. Staffell, D. Scamman, A. Velazquez Abad, P. Balcombe, P. E. Dodds, P. Ekins, N. Shah, K. R. Ward, *Energy Environ. Sci.* **2019**, *12*, 463–491.
[83] L. Fan, Z. Tu, S. H. Chan, *Energy Rep.* **2021**, *7*, 8421–8446.
[84] A. B. Stambouli, E. Traversa, *Renewable Sustainable Energy Rev.* **2002**, *6*, 433–455.
[85] O. Z. Sharaf, M. F. Orhan, *Renewable Sustainable Energy Rev.* **2014**, *32*, 810–853.
[86] K. Selvam, Y. Komatsu, A. Sciazko, S. Kaneko, N. Shikazono, *Energy Convers. Manage.* **2021**, *249*, 114839.
[87] Y. Kawabata, T. Nakajima, K. Nakamura, T. Hatae, Y. Tachikawa, S. Taniguchi, Y. Matsuzaki, K. Sasaki, *J. Power Sources.* **2020**, *448*, 227459.
[88] M. Dokiya, *Solid State Ionics.* **2002**, *152–153*, 383–392.
[89] M. Lo Faro, V. Antonucci, P. L. Antonucci, A. S. Aricò, *Fuel.* **2012**, *102*, 554–559.
[90] R. D. Farr, C. G. Vayenas J, *Electrochem. Soc.* **1980**, *127*, 1478.
[91] K. M. Nowicki, G. Carins, J. Bayne, C. Tupberg, G. J. Irvine, J. T. S. Irvine, *J. Mater. Chem. A* **2023**, *11*, 352–363.
[92] K. Miyazaki, H. Muroyama, T. Matsui, K. Eguchi, *Sustain. Energy Fuels* **2020**, *4*, 5238–5246.
[93] Q. Ma, R. Peng, L. Tian, G. Meng, *Electrochem. Commun.* **2006**, *8*, 1791–1795.
[94] A. Wojcik, H. Middleton, I. Damopoulos, J. Van herle, *J. Power Sources* **2003**, *118*, 342–348.
[95] G. G. M. Fournier, I. W. Cumming, K. Hellgardt, *J. Power Sources* **2006**, *162*, 198–206.
[96] Q. Ma, J. Ma, S. Zhou, R. Yan, J. Gao, G. Meng, *J. Power Sources* **2007**, *164*, 86–89.
[97] M. Han, X. Tang, H. Yin, S. Peng, *J. Power Sources* **2007**, *165*, 757–763.
[98] S. E. Wolf, F. E. Winterhalder, V. Vibhu, L. G. J. de Haart, O. Guillon, R.-A. Eichel, N. H. Menzler, *J. Mater. Chem. A* **2023**, *11*, 17977–18028.
[99] S. Zha, C. Xia, G. Meng, *J. Power Sources* **2003**, *115*, 44–48.
[100] D. Saebea, S. Authayanun, Y. Patcharavorachot, N. Chatrattanawet, A. Arpornwichanop, *Int. J. Hydrogen Energy* **2018**, *43*, 921–931.
[101] D. Kashyap, P. K. Patro, R. K. Lenka, T. Mahata, P. K. Sinha, *Ceram. Int.* **2014**, *40*, 11869–11875.
[102] F. Wang, Y. Lyu, D. Chu, Z. Jin, G. Zhang, D. Wang, *Mater. Sci. Technol.* **2019**, *35*, 1551–1562.
[103] P. Vinchhi, M. Khandla, K. Chaudhary, R. Pati Inorg, *Chem. Commun.* **2023**, *152*, 110724.
[104] L. Mathur, Y. Namgung, H. Kim, S.-J. Song, *J. Korean Ceram. Soc.* **2023**, *60*, 614–636.
[105] N. Jaiswal, K. Tanwar, R. Suman, D. Kumar, S. Upadhyay, O. Parkash, *J. Alloys Compd.* **2019**, *781*, 984–1005.
[106] M. B. Hanif, S. Rauf, M. Motola, Z. U. D. Babar, C.-J. Li, C.-X. Li, *Mater. Res. Bull.* **2022**, *146*, 111612.
[107] P. Hjalmarsson, M. Søgaard, M. Mogensen, *Solid State Ionics.* **2008**, *179*, 1422–1426.
[108] A. Endo, H. Fukunaga, C. Wen, K. Yamada, *Solid State Ionics.* **2000**, *135*, 353–358.

[109] T. Shimura, A. He, N. Shikazono J, *Electrochem. Soc.* **2019**, *166*, F821-F830.
[110] M. Oh, A. Unemoto, K. Amezawa, T. Kawada in Material stability, cation transport of La 0.6Sr 0.4Co 0.2Fe 0.8O 3-δ, in SOFC cathodic conditions, Vol. 35 (Ed. Eds.: Editor), City, **2011**, pp.2249–2253.
[111] M. A. Laguna-Bercero, J. A. Kilner, S. J. Skinner, *Chem. Mater.* **2010**, *22*, 1134–1141.
[112] K. Dumaisnil, J. C. Carru, D. Fasquelle, M. Mascot, A. Rolle, R. N. Vannier, *Ionics.* **2017**, *23*, 2125–2132.
[113] V. Vibhu, A. Rougier, C. Nicollet, A. Flura, J.-C. Grenier, J.-M. Bassat, *Solid State Ionics.* **2015**, *278*, 32–37.
[114] V. Vibhu, A. Rougier, C. Nicollet, A. Flura, S. Fourcade, N. Penin, J.-C. Grenier, J.-M. Bassat, *J. Power Sources* **2016**, *317*, 184–193.
[115] J.-M. Bassat, V. Vibhu, C. Nicollet, A. Flura, S. Fourcade, J.-C. Grenier, A. Rougier, *ECS Trans.* **2017**, *78*, 655–665.
[116] V. Vibhu, A. Flura, A. Rougier, C. Nicollet, S. Fourcade, T. Hungria, J.-C. Grenier, J.-M. Bassat, *J. Energy Chem.* **2020**, *46*, 62–70.
[117] Z. Xie, X. Feng, T. Zhang, Z. Wang, Y. Li, T. Chen, *Solid State Sci.* **2020**, *108*, 106356.
[118] D. Muñoz-Gil, M. T. Azcondo, C. Ritter, O. Fabelo, D. Pérez-Coll, G. C. Mather, U. Amador, K. Boulahya, *Inorg. Chem.* **2020**.
[119] S. Lü, X. Meng, X. Fu, M. Liu, Y. Sui, Y. Chen, J. Cao, Y. Sun, Y. Ji, L. Yang, *Int. J. Hydrogen Energy* **2020**.
[120] S. Park, S. Choi, J. Kim, J. Shin, G. Kim ECS, *Electrochem. Lett.* **2012**, *1*, F29–F32.
[121] S. Choi, S. Yoo, J. Kim, S. Park, A. Jun, S. Sengodan, J. Kim, J. Shin, H. Y. Jeong, Y. Choi, G. Kim, M. Liu, *Scientific Reports* **2013**, *3*, 2426.
[122] Z. Gao, L. V. Mogni, E. C. Miller, J. G. Railsback, S. A. Barnett, *Energy Environ. Sci.* **2016**, *9*, 1602–1644. <
[123] I. Sreedhar, B. Agarwal, P. Goyal, S. A. Singh J, *Electroanal. Chem.* **2019**, *848*, 113315.
[124] G. Yang, C. Su, H. Shi, Y. Zhu, Y. Song, W. Zhou, Z. Shao, *Energy Fuels* **2020**, *34*, 15169–15194.
[125] A. F. S. Molouk, J. Yang, T. Okanishi, H. Muroyama, T. Matsui, K. Eguchi, *J. Power Sources* **2016**, *305*, 72–79.
[126] M. Kishimoto, N. Furukawa, T. Kume, H. Iwai, H. Yoshida, *Int. J. Hydrogen Energy* **2017**, *42*, 2370–2380.
[127] O. A. Ojelade, S. F. Zaman, *Chem. Pap.* **2021**, *75*, 57–65.
[128] K. Xu, F. Zhu, M. Hou, C. Li, H. Zhang, Y. Chen, *Nano Res.* **2022**, *16*, 2454–2462.
[129] S. Oh, M. J. Oh, J. Hong, K. J. Yoon, H.-I. Ji, J.-H. Lee, H. Kang, J.-W. Son, S. Yang, *iScience.* **2022**, *25*, 105009.
[130] Y. Wang, J. Yang, J. Wang, W. Guan, B. Chi, L. Jia, H. Ying, Y. Xia, J. Chen, *ECS Trans.* **2019**, *91*, 1611.
[131] W. Akimoto, T. Fujimoto, M. Saito, M. Inaba, H. Yoshida, T. Inagaki, *Solid State Ionics.* **2014**, *256*, 1–4.
[132] Y. Song, H. Li, M. Xu, G. Yang, W. Wang, R. Ran, W. Zhou, Z. Shao, *Small.* **2020**, *16*, 2001859.
[133] S. Sorcar, H. Zinowits, E. P. Komarala, N. Moshe, I. Agranovich, B. A. Rosen, *J. Mater. Chem. A* **2022**, *10*, 24115–24126.
[134] G. Cinti, U. Desideri, D. Penchini, G. Discepoli, *Fuel Cells.* **2014**, *14*, 221–230.
[135] A. Hagen, H. Langnickel, X. Sun, *Int. J. Hydrogen Energy* **2019**, *44*, 18382–18392.
[136] S. Yu, Z. Wang, L. Yang, J. Liu, R. Guan, Y. Xiao, T. He, *Journal of the American Ceramic Society*, *n/a*.
[137] H. Shimada, Y. Yamaguchi, H. Sumi, Y. Mizutani *J, Electrochem. Soc.* **2020**, *167*, 124506.
[138] F. J. A. Loureiro, D. Pérez-Coll, V. C. D. Graça, S. M. Mikhalev, A. F. G. Ribeiro, A. Mendes, D. P. Fagg, *J. Mater. Chem. A* **2019**.
[139] K. D. Kreuer, *Annu. Rev. Mater. Res.* **2003**, *33*, 333–359.
[140] S. Hossain, A. M. Abdalla, J. H. Zaini, C. D. Savaniu, J. T. S. Irvine, A. K. Azad, *Int. J. Hydrogen Energy* **2017**, *42*, 27308–27322.
[141] I. Antunes, D. Pérez-Coll, N. Nasani, H. S. Soares, G. C. Mather, J. R. Frade, D. P. Fagg, *Int. J. Hydrogen Energy* **2021**, *46*, 13606–13621.
[142] E. Fabbri, L. Bi, D. Pergolesi, E. Traversa, *Adv. Mater.* **2012**, *24*, 195–208.
[143] C. Duan, R. Kee, H. Zhu, N. Sullivan, L. Zhu, L. Bian, D. Jennings, R. O'Hayre, *Nat. Energy* **2019**, *4*, 230–240.
[144] S. Choi, C. J. Kucharczyk, Y. Liang, X. Zhang, I. Takeuchi, H.-I. Ji, S. M. Haile, *Nat. Energy* **2018**, *3*, 202–210.
[145] H. Ding, W. Wu, C. Jiang, Y. Ding, W. Bian, B. Hu, P. Singh, C. J. Orme, L. Wang, Y. Zhang, D. Ding, *Nat. Commun.* **2020**, *11*, 1907.
[146] Q. L. Liu, K. A. Khor, S. H. Chan, *J. Power Sources* **2006**, *161*, 123–128.
[147] Y. Lin, R. Ran, C. Zhang, R. Cai, Z. Shao J Phys, *Chem. A* **2010**, *114*, 3764–3772.
[148] H. Tang, Z. Jin, Y. Wu, W. Liu, L. Bi, *Electrochem. Commun.* **2019**, *100*, 108–112.
[149] A. Grimaud, F. Mauvy, J. Marc Bassat, S. Fourcade, M. Marrony, J. Claude Grenier, *J. Mater. Chem.* **2012**, *22*, 16017–16025.
[150] Q. Wang, S. Ricote, M. Chen, *Electrochim. Acta* **2023**, *446*, 142101.
[151] L. Bi, S. Boulfrad, E. Traversa, *Chem. Soc. Rev.* **2014**, *43*, 8255–8270.
[152] A. Dubois, S. Ricote, R. J. Braun, *J. Power Sources* **2017**, *369*, 65–77.
[153] D. Han, N. Hatada, T. Uda, *J. Am. Ceram. Soc.* **2016**, *99*, 3745–3753.
[154] S. Robinson, A. Manerbino, W. Grover Coors, *J. Membr. Sci.* **2013**, *446*, 99–105.
[155] H. An, D. Shin, H.-I. Ji, *J. Korean Ceram. Soc.* **2018**, *55*, 358–363.
[156] M. Shang, J. Tong, R. O'Hayre, *RSC Adv.* **2013**, *3*, 15769–15775.
[157] K. Miyazaki, T. Okanishi, H. Muroyama, T. Matsui, K. Eguchi, *J. Power Sources* **2017**, *365*, 148–154.
[158] J. Yang, T. Akagi, T. Okanishi, H. Muroyama, T. Matsui, K. Eguchi, *Fuel Cells.* **2015**, *15*, 390–397.
[159] J. Yang, A. F. S. Molouk, T. Okanishi, H. Muroyama, T. Matsui, K. Eguchi, *ACS Appl. Mater. Interfaces* **2015**, *7*, 7406–7412.
[160] Y. Aoki, S. Kobayashi, T. Yamaguchi, E. Tsuji, H. Habazaki, K. Yashiro, T. Kawada, T. Ohtsuka, *J. Phys. Chem. C* **2016**, *120*, 15976–15985.
[161] Y. Pan, H. Zhang, K. Xu, Y. Zhou, B. Zhao, W. Yuan, K. Sasaki, Y. Choi, Y. Chen, M. Liu, *Appl. Catal. B* **2022**, *306*, 121071.
[162] H. Zhang, Y. Zhou, K. Pei, Y. Pan, K. Xu, Y. Ding, B. Zhao, K. Sasaki, Y. Choi, Y. Chen, M. Liu, *Energy Environ. Sci.* **2022**, *15*, 287–295.
[163] G. Meng, C. Jiang, J. Ma, Q. Ma, X. Liu, *J. Power Sources* **2007**, *173*, 189–193.
[164] X. Xiong, J. Yu, X. Huang, D. Zou, Y. Song, M. Xu, R. Ran, W. Wang, W. Zhou, Z. Shao, *J. Mater. Sci. Technol.* **2022**, *125*, 51–58.
[165] B. Stoeckl, V. Subotić, M. Preininger, M. Schwaiger, N. Evic, H. Schroettner, C. Hochenauer, *Electrochim. Acta* **2019**, *298*, 874–883.
[166] K. Xie, Q. Ma, B. Lin, Y. Jiang, J. Gao, X. Liu, G. Meng, *J. Power Sources* **2007**, *170*, 38–41.
[167] Q. Ma, R. Peng, Y. Lin, J. Gao, G. Meng, *J. Power Sources* **2006**, *161*, 95–98.
[168] F. Zhong, S. Yang, C. Chen, H. Fang, K. Chen, C. Zhou, L. Lin, Y. Luo, C. Au, L. Jiang, *J. Power Sources* **2022**, *520*, 230847.
[169] S. S. Shy, S. C. Hsieh, H. Y. Chang, *J. Power Sources* **2018**, *396*, 80–87.
[170] L. Liu, K. Sun, X. Wu, X. Li, M. Zhang, N. Zhang, X. Zhou, *Int. J. Hydrogen Energy* **2012**, *37*, 10857–10865.
[171] Y. Lin, R. Ran, Y. Guo, W. Zhou, R. Cai, J. Wang, Z. Shao, *Int. J. Hydrogen Energy* **2010**, *35*, 2637–2642.
[172] L. Zhu, C. Cadigan, C. Duan, J. Huang, L. Bian, L. Le, C. H. Hernandez, V. Avance, R. O'Hayre, N. P. Sullivan, *Commun. Chem.* **2021**, *4*, 121.
[173] F. He, Q. Gao, Z. Liu, M. Yang, R. Ran, G. Yang, W. Wang, W. Zhou, Z. Shao, *Adv. Energy Mater.* **2021**, *11*, 2003916.
[174] L. Zhang, W. Yang, *J. Power Sources* **2008**, *179*, 92–95.
[175] Y. Aoki, T. Yamaguchi, S. Kobayashi, D. Kowalski, C. Zhu, H. Habazaki, *Global Challenges.* **2018**, *2*, 1700088.
[176] G. Cinti, G. Discepoli, E. Sisani, U. Desideri, *Int. J. Hydrogen Energy* **2016**, *41*, 13583–13590.
[177] T. Okanishi, K. Okura, A. Srifa, H. Muroyama, T. Matsui, M. Kishimoto, M. Saito, H. Iwai, H. Yoshida, M. Saito, T. Koide, H. Iwai, S. Suzuki, Y. Takahashi, T. Horiuchi, H. Yamasaki, S. Matsumoto, S. Yumoto, H. Kubo, J. Kawahara, A. Okabe, Y. Kikkawa, T. Isomura, K. Eguchi, *Fuel Cells.* **2017**, *17*, 383–390.
[178] L. Barelli, G. Bidini, G. Cinti, *Energies.* **2020**, *13*, 6173.
[179] M. Zendrini, M. Testi, M. Trini, P. Daniele, J. Van Herle, L. Crema, *Int. J. Hydrogen Energy* **2021**, *46*, 30112–30123.
[180] M. Kishimoto, H. Muroyama, S. Suzuki, M. Saito, T. Koide, Y. Takahashi, T. Horiuchi, H. Yamasaki, S. Matsumoto, H. Kubo, N. Takahashi, A. Okabe, S. Ueguchi, M. Jun, A. Tateno, T. Matsuo, T. Matsui, H. Iwai, H. Yoshida, K. Eguchi, *Fuel Cells.* **2020**, *20*, 80–88.
[181] D. S. Dhawale, S. Biswas, G. Kaur, S. Giddey Inorg, *Chem. Front.* **2023**, *10*, 6176–6192.
[182] A. Valera-Medina, H. Xiao, M. Owen-Jones, W. I. F. David, P. J. Bowen, *Prog. Energy Combust. Sci.* **2018**, *69*, 63–102.
[183] D. Kwak, Y. Lei, R. Maric, *Talanta.* **2019**, *204*, 713–730.
[184] A. Kumar, R. Meunier-Prest, F. Herbst, O. Heintz, E. Lesniewska, M. Bouvet, *Chem. Eng. J.* **2022**, *436*, 135207.
[185] A. Kumar, R. Meunier-Prest, E. Lesniewska, M. Bouvet, *Sens. Actuators B* **2022**, *369*, 132313.
[186] S. Ouedraogo, R. Meunier-Prest, A. Kumar, M. Bayo-Bangoura, M. Bouvet, *ACS Sens.* **2020**, *5*, 1849–1857.
[187] L. Di Zazzo, A. Kumar, R. Meunier-Prest, C. Di Natale, R. Paolesse, M. Bouvet, *Chem. Eng. J.* **2023**, *458*, 141465.

[188] A. Kumar, N. Alami Mejjati, R. Meunier-Prest, A. Krystianiak, O. Heintz, E. Lesniewska, C. H. Devillers, M. Bouvet, *Chem. Eng. J.* **2022**, *429*, 132453.
[189] Z. Şahin, R. Meunier-Prest, F. Dumoulin, A. Kumar, Ü. Isci, M. Bouvet, *Sens. Actuators B* **2021**, *332*, 129505.
[190] S. Ganesh Moorthy, B. King, A. Kumar, E. Lesniewska, B. H. Lessard, M. Bouvet, *Advanced Sensor Research.* **2023**, *2*, 2200030.
[191] G. Bengasi, R. Meunier-Prest, K. Baba, A. Kumar, A. L. Pellegrino, N. D. Boscher, M. Bouvet Adv, *Electron. Mater.* **2020**, *6*, 2000812.
[192] P. S. Chauhan, S. Bhattacharya, *Int. J. Hydrogen Energy* **2019**, *44*, 26076–26099.
[193] L. Wen, Z. Sun, Q. Zheng, X. Nan, Z. Lou, Z. Liu, D. R. S. Cumming, B. Li, Q. Chen, *Light-Sci. Appl.* **2023**, *12*, 76.
[194] T. K. N. Pham, J. J. Brown, *ChemistrySelect.* **2020**, *5*, 7277–7297.
[195] H. Iwai, M. Saito, Y. Yamamoto, K. Inaoka, S. Suzuki, Y. Takahashi, in *Stability of Materials for Solid Oxide Fuel Cells with Ammonia Fuel, Vol.*, **2017**, pp.123–126.
[196] J. Yang, A. F. S. Molouk, T. Okanishi, H. Muroyama, T. Matsui, K. Eguchi, *ACS Appl. Mater. Interfaces* **2015**, *7*, 28701–28707.
[197] H. Kobayashi, A. Hayakawa, K. D. Kunkuma A Somarathne, Ekenechukwu C. Okafor, *Proc. Combust. Inst.* **2019**, *37*, 109–133.

Manuscript received: December 28, 2023
Revised manuscript received: March 16, 2024
Version of record online: ■■, ■■

REVIEW

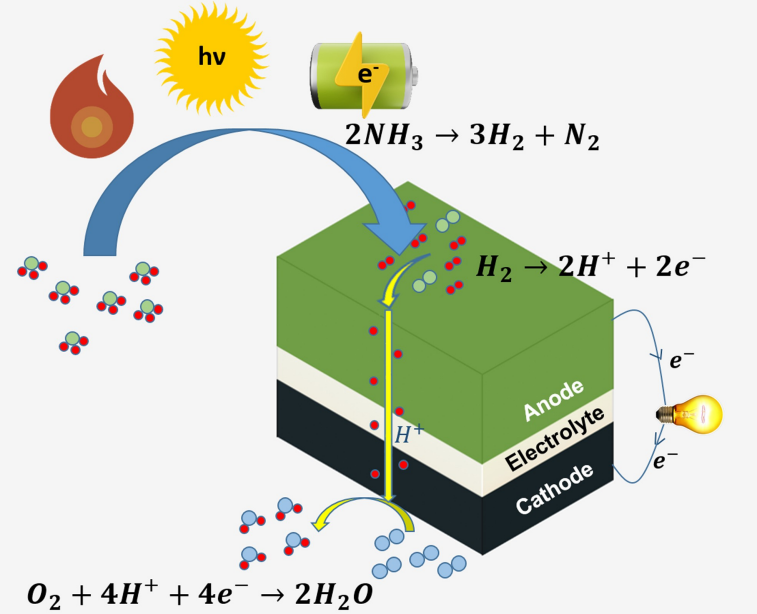

A. Kumar, V. Vibhu, J.-M. Bassat, L. Nohl, L. G. J. de Haart, M. Bouvet*, R.-A. Eichel*

1 – 31

Ammonia as a Potential Energy Vector in the Burgeoning Hydrogen Economy

In this review, recent advances in the development of ammonia decomposition methods, such as thermocatalytic, oxidative, electrocatalytic and photocatalytic processes are presented. Moreover, recent progress in direct ammonia SOFC technology using various catalyst materials, including electrochemical performance, process analysis and long-term durability are reviewed and discussed.